Full Length Article

Hydrocracking of surgical face masks over Y Zeolites: Catalyst development, process design and life cycle assessment

Muhammad Usman Azam [a], Auguste Fernandes [b], Inês Graça [a,*], Waheed Afzal [a,*]

[a] School of Engineering, University of Aberdeen, Aberdeen AB24 3UE, Scotland, UK
[b] Centro de Química Estrutural, Institute of Molecular Sciences, Instituto Superior Técnico, Universidade de Lisboa, Av. Rovisco Pais, 1049-001 Lisboa, Portugal

A B S T R A C T

This study highlights the hydrocracking route for the management of surgical face masks, made of polypropylene, into liquid fuels. Hydrocracking experiments were performed at 325 °C and 10 bar cold H_2 pressure over Ni-loaded HY and steamed HY zeolites. Ni-loaded steamed Y zeolite demonstrated to be the best catalyst leading to considerably high conversion (100 wt%) and selectivity to liquids (85.5 wt%). The increase in the external surface area and mesoporous volume that improved the bulk polymer molecules diffusion, combined with the uniformly dispersed Ni particles and the additionally generated Lewis acidity, were at the origin of the observed behaviour. This catalyst also showed reasonable stability and ability to be thermally regenerated. From the environmental perspective, life cycle assessment shows the benefits of hydrocracking over pyrolysis and incineration. Therefore, our results demonstrate that Ni-loaded steamed Y zeolites could be promising catalysts for the upcycling of surgical face masks to gasoline range fuels, with minimum environmental impacts.

1. Introduction

The COVID-19 pandemic has urged demand and utilization of personal protective equipment, most prominently surgical face masks that are primarily polymeric material (i.e., polypropylene), significantly exacerbating the infectious plastic problem [1]. Globally, 52 billion face masks were manufactured in 2020 [2] and, according to an estimation by the United Nations, a large share of these masks ended up in landfills or in our oceans [3]. Therefore, what originated as a shield against the infectious disease eventually transformed into a serious scarcity of economy and environment and now, the world is on the doorstep of a massive waste pandemic. To counter this problem, incineration has been widely employed to manage the waste surgical face masks problem [4]. Although the energy (i.e., heat of combustion) from this process can be utilized directly to generate steam and/or electricity [5], notable amounts of particulate matter, greenhouse gases, and furans are generated as by-products. This makes this operation less favourable [6]. Moreover, the heterogeneous composition of surgical face masks and prior requirement of sufficient disinfection makes it challenging and complex to mechanically recycle them [7]. Therefore, developing a viable solution for the management of surgical face masks with the least environmental footprints is essential.

Surgical face masks being the derivative of polypropylene have high economic and heating value. Tertiary recycling of these polymeric materials into alternative chemical intermediates such as gases and/or liquid products may provide a sustainable approach for the management of waste surgical face masks. These intermediates are also suitable to utilize as feedstocks for the re-production of surgical face masks, petrochemicals, and/or other value-added chemicals [8]. Recently, Chalermsinsuwan et al. [9] studied the gasification of medical masks for hydrogen production. However, the high reaction temperature and heat energy requirements (i.e., 900 °C) of the process make it energy-inefficient with high capital cost. Similarly, Aragaw et al. [10] and Li et al. [11] reported the pyrolysis of waste face masks into pyrolysis oil. However, the highly acidic and corrosive nature of pyrolysis oil makes it difficult to store and poses a considerable risk of damaging engines and other processing equipment. Furthermore, the high-temperature requirements (500–800 °C), production of highly unsaturated products, mass and heat transfer limitations make this process unstable and lead to certain industrial problems [12]. On the other hand, hydrocracking may address the aforementioned concerns of gasification and pyrolysis. This process has recently drawn notable attention because of modest reaction conditions (i.e., 300–400 °C) and is a promising way of converting waste plastics into saturated liquid products [13,14]. Moreover, the

introduction of hydrogen conditions (i.e., 5–20 bar) allows the reduction of coke precursors, as well as the extraction of heteroatoms i.e., fluorine, bromine, and chlorine from plastics [13,15]. In addition, compared to non-catalytic hydrocracking, catalytic hydrocracking reveals considerable importance, as not only it decreases the reaction time and temperature, but also significantly enhances the conversion of waste plastics into relatively lower boiling range liquid hydrocarbons [16]. Generally, a bifunctional catalyst, composed of an acidic support for cracking of long chain polymers and a metal function where the hydrogenations-dehydrogenations take place, is utilized [17]. Up to now, researchers have fabricated and used distinct types of catalysts with a combination of metals over acidic supports to perform the hydrocracking reaction.

Usually, elements from the VIIB group, such as Pt or Pd [18,19] and transition metals, including Mo, Ni, W, and Co [15,20] have been employed as metal components, while microporous zeolites (H-ZSM5, H-Beta, H-USY) [17], sulfated zirconia (ZrO_2/SO_4^{-2}) [18], and silica-alumina (SiO_2/Al_2O_3), [21] etc. have been utilized as acidic supports. Among them, crystalline zeolites are undoubtedly the most extensively utilized and reported acidic supports because of their porous structure, crystallinity, acidic strength, long-term stability, exceptional activity, and selectivity predominately towards gasoline range oils [22,23]. However, the acidic and physiochemical properties of zeolites become worthless when addressing the hydrocracking of bulky polymers due to microporosity and diffusion problems. In line with this, the catalytic activity of these microporous zeolites can significantly be enhanced by decreasing the intracrystalline diffusion constraints in micropores and channels [24]. A number of potential solutions, such as the formation of ultra-large porous zeolites, zeolites with nanocrystals, and synthesis of hierarchical zeolites, have been proposed [25]. However, the limited structural stability, less acidity, and high pricing of the templates and surfactants employed in the synthesis of ultra-large porous zeolites have restricted their applications at an industrial scale. Similarly, nanocrystal zeolites suffer from several challenges, as their synthesis involves the utilization of a significant quantity of toxic and expensive templates with severe environmental impact [26]. Also, fabrication of hierarchical zeolite, with modified acidity, crystallinity, and enhanced multilevel porosities, using dealumination technique, might be considered as a promising approach. However, if not controlled, the dealumination procedure may sacrifice part of the zeolite framework (i.e., removal of framework Al) which results in loss of crystallinity, acidity, and uncontrollable secondary porosity [27].

In addition, the benefits of hydrocracking of waste surgical face masks over linear end of life and other circular end of life waste plastics management options need to be quantified using life cycle assessment. This is the most logical and viable methodology for assessing impact of any material or process on environment. Moreover, systemized actions are required to limit different environmental impacts and to examine how the assembling and processing activities associated with plastics, their transportation, and management operations affect the climate.

Herein, a commercial HY zeolite was used as acidic support for the hydrocracking of waste surgical face masks, made of polypropylene. In addition, a HY zeolite with enhanced porosity and surface area was fabricated by mild steaming. Mild steaming conditions were applied to try to improve the diffusion of the bulky plastic molecules and, so, the activity of the catalysts, without compromising the framework crystallinity, acidity, stability and hierarchical pore structures. Kung et al. [28] and Masuda et al.[29] both reported the significance of mild steaming for the enhancement in activity of zeolite for hydrocarbon cracking. Moreover, Pham et al., [30] observed that the steaming at 480 °C for 4 h enhanced the mobility of EFAL to create synergistic sites that improved the activity of the zeolite by 1.75 times. The impact of adding a metallic function (Ni) to the parent zeolite Y and to the steamed zeolite, as well as the influence of the metal content, on the catalytic hydrocracking of waste surgical face masks were investigated. The performance of each catalytic system was evaluated in terms of product distribution. The best catalyst found in this study was assessed for stability and reusability.

Moreover, based on the experimental results, this study aims at accessing the potential environmental impacts of hydrocracking of waste surgical face masks and comparing the results with multiple other scenarios, using life cycle assessment (LCA) approach, which not only compares and distinguishes the ecologically most effective waste surgical face masks management alternative, but also calculates environmental impact assessment of all materials and processes based on ISO standards.

2. Experimental

2.1. Materials and reactants

Three-layer virgin surgical face masks (non-sterile) were supplied by Medisave UK and utilized for the hydrocracking reactions. HY zeolite with a Si/Al ratio of 30, and nickel nitrate hexahydrate ($Ni(NO_3)_2 \cdot 6H_2O$ with 99% purity) were employed for catalyst synthesis. In addition, both n-heptane (99%) and tetrahydrofuran (THF, 99%) were utilized for solvent extraction. All these chemicals were purchased from Alfa Aesar.

2.2. Preparation of the steamed Y zeolite

The steaming of the parent HY zeolite was performed at 500 °C for 4 h. For this, 100 mL.min^{-1} of nitrogen was saturated with water and contacted with the parent zeolite. The as-synthesized steamed zeolite was denoted as ST-HY.

2.3. Preparation of Ni impregnated Y zeolite

Ni impregnated HY zeolite samples were prepared using incipient wetness impregnation. Different metal-based zeolite samples with loadings of 2, 5 and 10 wt% of Ni were prepared with a dropwise addition of aqueous solution of nickel nitrate hexahydrate (Ni $(NO_3)_2 \cdot 6H_2O$) to the dried HY zeolites. The obtained paste like samples were air-dried at 100 °C overnight in an oven, followed by calcination at 500 °C under air flow of 60 mL.min^{-1}.g^{-1} for 6 h. These HY zeolites were denoted as 2 %Ni-HY, 5 %Ni-HY and 10 %Ni-HY. Similarly, the optimized quantity of Ni (5 wt% of Ni) was used to fabricate Ni impregnated steamed zeolite sample using the same method. This sample was denoted as 5 %Ni-ST-HY (Ni impregnated steamed HY zeolite). Before being used, all the Ni impregnated samples were pre-reduced in a tubular furnace with a hydrogen flow of 100 mL.min^{-1}. g^{-1} for 2 h, at 500 °C. The selection of the pre-reduction temperature was based on the experimental H$_2$-TPR results.

2.4. Catalyst characterization

Various analytical and imaging techniques were employed for the characterization of the parent and modified zeolite samples, as well as of the surgical face masks.

X-ray diffraction (XRD) of the calcined and pre-reduced zeolites was conducted on a PANalytical X'Pert X-ray Powder diffractometer (PIXcel 1D detector) using Cu Kα as a radiation source, a 2θ range of 5-90° and a scanning step of 0.02°/5 s. In addition, the relative intensity of all samples was estimated by comparing the area under the XRD curves for a 2θ range from 5 to 30° to those of the pristine zeolite Y, which was assumed to be 100 %. The framework Si/Al ratios of pristine and steamed HY zeolites were computed using the unit cell parameter ($a_0 = 24.233$ Å for HY zeolite and $a_0 = 24.235$ Å for steamed HY zeolite), using the Breck-Flanigen equation [31]. The elemental analysis for the composition of Si and Al of both calcined parent and steamed HY zeolites was determined by Inductively Coupled Plasma-Optical Emission Spectroscopy (ICP-OES).

Ni particle size, metal dispersion, and the detailed morphology of the pre-reduced catalysts were studied by Transmission Electron Microscopy (JEOL 1400 plus TEM). The equipment was operated at an

accelerating voltage of 120 kV for the microstructure characterization and ImageJ software was used to calculate the average particle size of the visible Ni particles.

N$_2$-physisorption was carried out in a Tristar-3000 apparatus (Micromeritics) at −196 °C. Ni-loaded samples were pre-reduced before analysis. All the samples were degassed under nitrogen at 350 °C overnight prior to analysis. The microporosity (V$_{micro}$) and external surface area were calculated utilizing the t-plot (Harkins and Jura) method, while the total pore volume (V$_{total}$) was derived from the adsorbed quantity of N$_2$ at a relative pressure (P/P$_o$) of 0.97. The mesopore volume (V$_{meso}$) was determined as the difference between V$_{total}$ and V$_{micro}$.

Hydrogen temperature programmed reduction (H$_2$-TPR) was performed using a TPDRO 1100 instrument for the calcined Ni impregnated zeolites. Before analysis, Ni loaded zeolite samples were pre-treated under nitrogen with a flow rate of 20 mL.min^{-1} at 200 °C and then cooled to 40 °C. After that, the samples were reduced by running a 5% H$_2$/N$_2$ mixture with a flow rate of 20 mL.min^{-1} from 40 °C to 900 °C at 10 °C.min^{-1}. A thermal conductivity (TCD) detector was used to assess the quantity of H$_2$ consumed.

The nature, quantity and strength of the acidic sites of pristine HY zeolite, steamed HY zeolite and Ni loaded samples, after calcination, were analysed by pyridine adsorption followed by FTIR spectroscopy using a Nicolet Nexus spectrometer. Powdered samples were used to produce thin wafers of 10–20 mg.cm^{-2} thickness. The as-prepared self-supported wafers were pre-treated under vacuum (10^{-3} Pa) for 2 h at 450 °C and the IR spectra of the samples before pyridine adsorption were taken. Later, the samples were cooled down to 150 °C and subjected to excess pyridine vapour (200–300 Pa) adsorption for 10 min followed by the removal of pyridine for 30 min under vacuum and the IR spectrum with adsorbed pyridine was recorded. Afterwards, the temperature of the cell was elevated under secondary vacuum to 250, 350 and 450 °C and the spectra at each temperature were recorded after half an hour to analyze the strength of the acid sites of the catalysts.

DRS spectra in the UV–vis region were obtained for the calcined samples in a Varian Cary 5000 UV–Vis-NIR spectrophotometer, equipped with a Praying Mantis™ Diffuse Reflection Accessory, in the 200–800 nm range, using a spectral bandwidth of 4 nm and a scan rate of 600 nm/s. In order to assess the presence of different Ni species, the Schuster-Kubelka-Munk (SKM) function, F(R), was applied to each reflectance spectrum, and the results were plotted against wavelength. The reflectance, at each wavelength, was used to determine the SKM function.

$$F(R) = \frac{(1-R)^2}{2R}, \qquad (1)$$

where R is the ratio of the sample's and the standard's light reflection intensities.

The thermogravimetric analysis (TGA) of the surgical face masks was accomplished using a TGA/DSC 3 + system from Mettler Toledo. First of all, the virgin surgical face masks were shredded to a manageable size for use with the instrument crucible. A few mg of the shredded samples were placed in already weighted alumina crucibles, and the samples were heated up from 25 to 900 °C at 10 °C.min^{-1} under nitrogen atmosphere. Similarly, the coke content on the spent 5% Ni-ST-HY zeolite samples after first and second reaction runs were analysed using the same TGA equipment from 25 to 900 °C with a temperature ramp of 10 °C.min^{-1} under air flow of 10 mL.min^{-1}.

The chemical composition and the polymeric type of 3-ply surgical face masks were performed using attenuated total reflection (ATR) Fourier Transformed Infrared (FTIR) apparatus (Perkin-Elmer 1750 series spectrometer). Infrared (IR) spectra of all three sides of surgical face masks were examined without any preparation at room temperature in the range of 4000–400 cm^{-1}.

2.5. Hydrocracking experiments

Hydrocracking was performed in a high-pressure, stainless steel, cylindrical Parr reactor (5500 compact series). Before the experiment, surgical face masks were shredded into 2–2.5 mm pieces. Both shredded surgical mask and catalyst were first dried in an oven and later introduced into the reactor vessel in a ratio of 10:1 (g/g). Then the vessel was tightly connected to the reactor head and purged first with N$_2$ and then with H$_2$ at 10 bar. An initial hydrogen pressure of 10 bar and a temperature setpoint (325 °C) were given to the reactor followed by turning on the heating system. Typically, hydrocracking temperatures at an industrial level vary in the range 300–450 °C [32]. Therefore, a temperature closer to the minimum temperature of the range was selected to allow for the cracking to take place, avoiding secondary cracking that would increase gases formation at the expense of mid-range liquid products (gasoline and diesel). In addition, the selection of a lower temperature for the hydrocracking could be beneficial to reduce energy inputs of the process. The feed and catalyst particles were mechanically mixed using an agitator assembly which moved at 1000 rpm. When the temperature reached the set value, the reaction time was started. The reaction was performed for 2 h before the furnace was switched off. The reactor was allowed to cool down to room temperature and after that gaseous, liquid, and solid products were collected.

Solvent extraction principle was employed to analyse the reaction products. After the extraction of the gaseous products, a known amount of n-heptane was introduced to the reaction vessel which contained liquid and solid products. The n-heptane was used to extract the lighter liquid products, denoted as "oils", whereas the heavier oil products were dissolved in tetrahydrofuran (THF). Both lighter and heavier oils are collectively categorised as liquids. The THF insoluble part which contained a fraction of coke along with unreacted plastics and catalyst was dried and called solids after subtracting the amount of catalyst.

To know the product composition towards gasoline and diesel ranges based on the carbon number, the oil mixture was combined with a known quantity of ethyl acetate as an external standard and analyzed by gas chromatography (GC). A RASTEK chromatograph, equipped with an Agilent DB-1 capillary column of 50 m length and a flame ionisation detector, was used.

The following five equations were used to calculate the overall conversion and the percentage of mass yields of the products.

$$Y_{oils} = \frac{weight\ of\ n\text{-}heptane\ solubles}{weight\ of\ the\ mask} \times 100 \qquad (2)$$

$$Y_{heavierOils} = \frac{weight\ of\ total\ THF\ solubles}{weight\ of\ the\ mask} \times 100 \qquad (3)$$

$$Y_{solids} = \frac{weight\ of\ the\ dried\ solid\ residue}{weight\ of\ the\ mask} \times 100 \qquad (4)$$

$$Y_{gases} = 100 - (Oil\ Yield + Liquid\ Yeild + Solid\ Yield) \qquad (5)$$

$$C = \frac{Weight\ of\ mask - weight\ of\ solid\ residue}{Weight\ of\ the\ mask} \times 100 \qquad (6)$$

where Y is the yield of product and C is the conversion. Similarly, the selectivity of the products were calculated as

$$S_i = \frac{Y_i}{C} \times 100 \qquad (7)$$

where C is the conversion, S and Y correspond to the selectivity and yield of ith product respectively (i.e., *i* represents the gaseous/lighter oils and/or heavier oils).

The stability and regeneration of the best performing catalyst were also studied for the hydrocracking experiments. To assess the stability, three consecutive reaction runs were performed. After each reaction run, the catalyst was recovered, washed and filtered with acetone, dried

overnight at 100 °C and used again in the following run. To investigate the ability of the catalyst to be regenerated, the spent catalyst after the third reaction cycle was recovered, washed and filtered with acetone, dried overnight at 100 °C, calcined in air followed by reduction under hydrogen flow at 500 °C, under the same conditions as explained in section 2.3, to clean the catalyst surface. All the experiments were duplicated under same reaction conditions and the average values were reported with a relative error of ± 10%.

3. Results and discussion

3.1. Fresh catalyst characterization

The XRD diffractograms of the parent and steamed HY zeolite samples with and without the different loadings of Ni are shown in Fig. 1a. All the samples present the diffraction peaks at 2 θ of 6.2°, 10.3°, 12.1°, 15.9°, 18.9°, 20.7°, 24°, 27.5°, which coincide with the faujasite (FAU) zeolitic structure [33]. Ni-loaded zeolites also show a comparable pattern to the parent HY zeolite, demonstrating that the zeolite structure was not significantly altered throughout the impregnation process (Fig. 1b). For lower Ni loadings, it is not possible to see the diffraction peaks corresponding to the presence of Ni species. In fact, at low Ni contents, this metal might escape the XRD detection or might be present as small and well dispersed Ni particles. After 10 wt% Ni impregnation, the diffractogram shows very small XRD peaks at 37.3°, 43.5° and 62.9°, characteristics of NiO species. This might indicate the presence of slightly larger Ni particles with the increase in the Ni content, as further confirmed by TEM images (Fig. 2). However, the small peak size still

indicates the presence of relatively small Ni particles. Moreover, Table 1 shows the relative intensity of the steamed HY zeolite and Ni-loaded catalysts to those of pristine HY zeolite. Only a very small loss of intensity is observed for the steamed HY zeolite, which indicates a negligible decrease in the relative crystallinity of the zeolite, confirming that the steaming process was not aggressive for the zeolite framework. A slight intensity loss is also observed with the addition of Ni to the framework and the reduction is more evident for higher Ni loadings, which is not strange considering that the added Ni will also absorb the XRD radiation. Upon reduction of the Ni catalysts (Fig. 1b), the positions of the peaks shifted slightly due to the changes in the crystal structure. The 10% Ni-HY exhibits diffraction peaks at 44.6° and 51.9° assigned to the presence of Ni° metallic particles [34]. However, as previously said, these low intensity peaks were not clear in all other Ni loaded zeolites and steamed zeolite due to low quantity of Ni loading and this is in accordance with previous literature [15].

Additionally, Table 1 presents the global and framework Si/Al ratios, and the number of extra-framework aluminium (EFAL) species of both parent and steamed HY zeolites based on the structure of the FAU. It can be seen that the parent and the steamed HY zeolites show almost similar framework Si/Al ratios. This confirms that the steaming treatment performed did not cause the removal of framework aluminium, which agrees with the non-decrease of the Brønsted acidity, as it will be observed later in this paper. Considering that the silicon on the zeolite remains the same before and after the treatment, the number of EFAL was estimated for both samples based on the global and framework Si/Al ratios. The results show that the steaming treatment seems to be responsible for the removal of a small number of EFAL species from the zeolite, which is also consistent with the small decrease in Lewis acid sites after steaming (shown later in this paper). With the removal of EFAL from the zeolite an increase in the global Si/Al ratio of the zeolite would be expected after the steaming procedure. However, global Si/Al ratios are identical for both parent and steamed HY zeolites. This could be due to the fact that the parent zeolite already presents a very small number of EFAL species, so that any small removal of these would not have a significant impact on the global Si/Al. Taking into account the mild steaming conditions applied, results obtained are not strange as it is generally more challenging to remove framework aluminium when the zeolite has a higher Si/Al ratio [35]. In addition, it has been recently shown by Pham et al. [30] that the activation energy required for the framework aluminium hydrolysis is typically much larger than the one needed for the EFAL migration under steaming conditions.

Table 1 also shows the microporous volume, mesoporous volume and external surface area of the zeolites. First of all, it is possible to see that the parent HY zeolite already presents a considerable mesoporosity, which will be important for the hydrocracking of the bulky polymer molecules in the surgical face masks. It is also worth noting that the steaming treatment of the parent HY zeolite increased the mesoporosity and external surface area, as expected. Interestingly, the micropore volume also increased with the steaming which might be because of the removal of some debris (i.e., extra-framework Al as previously observed) from the structure during steaming. Overall, impregnation of the HY zeolite with Ni led to a reduction in the microporous and mesoporous volumes and external surface area, the effect being more pronounced at higher Ni contents and especially at 10 wt% Ni. This indicates an increase in the Ni particle size with the increase in the Ni amount, as in agreement with the XRD results and previous reports [15]. Addition of 5 wt% of Ni to the steamed HY zeolite also conducted to a decrease in the microporous volume and mesoporous volume of the zeolite. However, no change of the external surface area took place, contrary to what happened for the HY zeolite for the same amount of Ni (5 wt%). This might reveal that the Ni particles are mostly located inside the zeolite structure in the case of the steamed HY zeolite.

Fig. 2 shows the TEM results obtained for the different Ni-loaded HY zeolites and Ni loaded steamed HY zeolite. HY samples containing 2 and 5 wt% of Ni show a combination of relatively small Ni particles with
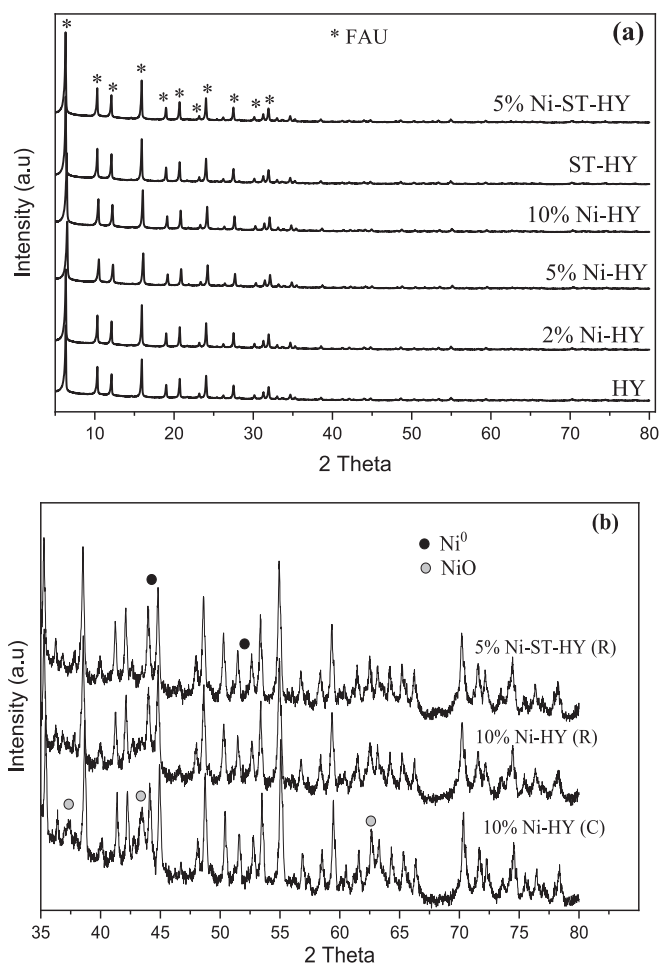
Fig. 1. (a) XRD diffractograms of HY and modified samples (b) Identification of NiO and Ni° species on XRD diffractograms; R: reduced, C: calcined.
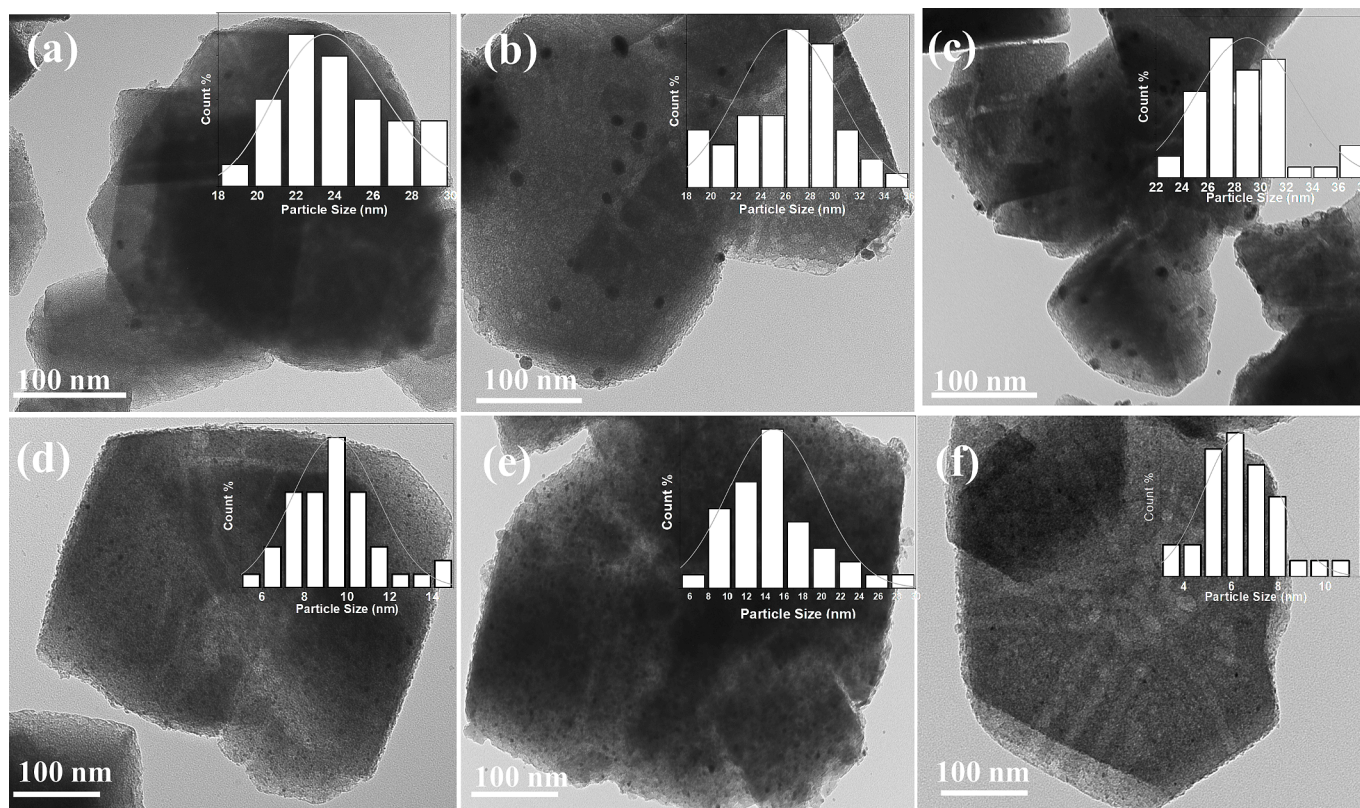
Fig. 2. TEM images of (a) 2% Ni-HY, (b) 5% Ni-HY, (c) 10% Ni-HY, (d) 5% Ni-ST-HY, (e) spent 5% Ni-ST-HY catalyst after 3rd run and (f) regenerated 5% Ni-ST-HY catalyst.

Table 1
Relative XRD intensity (or crystallinity), acidic properties and textural properties of the zeolite samples.

Catalyst Name	Relative intensity (%)	Si/Al[a]	Si/Al[b]$_{IV}$	EFAL	Brønsted acid sites ($\mu mol.g^{-1}$)	Lewis acid sites ($\mu mol.g^{-1}$)	Total acidity ($\mu mol.g^{-1}$)	V_{micro} ($cm^3.g^{-1}$)	V_{meso} ($cm^3.g^{-1}$)	S_{ext} ($cm^3.g^{-1}$)
HY	100	30.44	40	1.4	232	45	277	0.239	0.248	256
2% Ni-HY	99	–	–	–	167	185	352	0.224	0.243	263
5% Ni-HY	97	–	–	–	121	267	388	0.227	0.224	241
10% Ni-HY	94	–	–	–	119	286	405	0.186	0.198	214
ST-HY	95	30.50	37	1.1	243	40	283	0.272	0.283	297
5% Ni-ST-HY	92	–	–	–	98	208	306	0.252	0.267	296
Spent Catalyst (3rd Run) [c]	–	–	–	–	–	–	–	0.152	0.193	206
Regenerated Spent Catalyst [c]	–	–	–	–	–	–	–	0.222	0.232	259

V_{micro} micropore volume; V_{meso} mesopore volume; S_{ext} external surface area; EFAL extra-framework aluminium species.

[a] Global Si/Al determined from elemental analysis (ICP-OES).

[b] Framework Si/Al calculated from the unit cell parameter ($a_0 = 24.233$ Å for Y zeolite and $a_0 = 24.235$ Å for steamed Y zeolite), using the Breck-Flanigen equation [31].

[c] Refers to 5% Ni-ST-HY catalyst.

occasional larger ones on the surface. This explains the lower reduction in the textural properties with the addition of these Ni contents. However, with the increase of the Ni loading to 10 wt%, a higher amount of larger Ni particles can be seen on the outer surface of the zeolite, which is also consistent with the N$_2$ physisorption and XRD data. Average Ni particle size for the 2, 5 and 10 wt% Ni on the HY zeolite were estimated to be 23, 26 and 29 nm respectively. Interestingly, in the case of the steamed Y zeolite, the Ni size distribution appears to be more uniform all over the zeolite, showing an average particle size of 9 nm. Even though it may not be possible to observe the smallest Ni particles at much deeper zeolite locations by TEM given the apparatus resolution, the fact that these Ni particles are much smaller for the steamed zeolite could indicate that more particles are located inside the zeolite framework, which

would be consistent with the N$_2$ physisorption data for the 5% Ni-ST-HY catalyst and later with the H$_2$-TPR results. In addition, the better dispersion of Ni on the steamed HY zeolite may be due to the relative increase in the textural properties (14–16 %) of this zeolite when compared to the HY zeolite and to the change in the surface microchemical environment of the zeolite. In fact, the steaming performed on the HY zeolite led to the removal of extra-framework aluminium species, which may have altered the electronic charge distribution on the zeolite surface with an impact on the Ni dispersion.

The existence of various Ni species and their reducibility on the zeolitic framework can be determined by H$_2$-TPR through observing the peaks that arise at different temperatures in relation to various reduction sites. According to the literature, H$_2$-TPR peaks below 450 °C represent

the presence of NiO particles on the outer surface of the zeolite. The detected values in the intermediate temperature ranges of 500–600 ℃ are attributed to the reduction of Ni^{2+} at the supercages, whereas any peak at about 600 and 800 ℃ correspond to Ni^{2+} at the sodalite cages and hexagonal prisms respectively [15]. Based on the H_2-TPR results in Fig. 3, it can be seen that Ni can be found almost equally in all the positions of the framework, except the hexagonal prisms, at 2 wt% Ni content. On the other hand, the dominant position for Ni appears to be the supercages when increasing the amount to 5 wt%. As expected, the amount of NiO on the external surface of the pristine zeolite increased with the increase in Ni-loading, being especially important at 10 wt% Ni loading. This agrees with the increase in the Ni particle size observed while increasing the Ni loading. In case of the steamed HY zeolite, Ni is mainly located within the supercages, similarly to what happen for the 5% Ni-HY since they present the same Ni content. However, almost no Ni can be found on the outer surface of the steamed zeolite when compared to the 5% Ni-HY. This is also consistent with the TEM and N_2 physisorption data, and with the previous literature [15,36]. Once again, the presence of smaller Ni particles agrees with deeper framework locations, within the micro- and mesopores, and more specifically in the supercages of the zeolite.

Fig. 4 depicts the DRS UV–Vis spectra for the Ni-impregnated zeolite samples. Samples containing 2, 5 and 10 wt% Ni impregnated on the HY zeolite have a main massif between 250 and 350 nm. Additionally, other small bands can be seen at about 380, 420, 560, 715 and 760 nm. These bands indicate that the dominant Ni species on these samples is NiO. Indeed, according to the literature [37] the bulk NiO typically presents UV–Vis bands at about 200, 270, 350, 388, 420, 470, 560, 640, 725 and 780 nm. On the other hand, the 5% Ni steamed HY zeolite has a main UV–Vis massif centred at about 400 nm. This may result from the combination of bands associated with the presence of octahedral Ni^{2+} particles in exchange positions and NiO. In fact, the d-d spin-allowed electronic transitions of octahedrally coordinated Ni^{2+} species can normally be seen at about 400 nm [37], while NiO has bands at 380 and 420 nm as previously mentioned. The presence of the octahedrally coordinated Ni^{2+} in this sample can also be confirmed by the appearance of a small band at 650 nm [37]. Another small band at around 250 nm also appears in the 5%-Ni-ST-HY zeolite spectrum, which is related to NiO.

Fig. 5a shows the FTIR spectra in the hydroxyl region (3800–3500 cm^{-1}) of the parent HY zeolite, steamed HY zeolite and their Ni loaded samples. All the spectra displayed are identical, but with some differences in the intensities of the three main bands. The bands at 3565 and 3630 cm^{-1} are attributed to the Brønsted acidic sites and appear due to
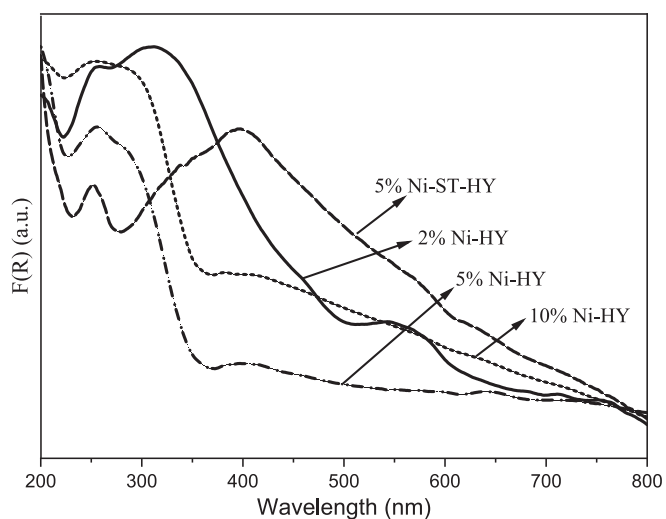

Fig. 4. DRS-UV–Vis spectra for the Ni-loaded HY zeolite and steamed HY zeolite sample.

the vibration of the bridging hydroxyl groups (Al-OH-Si) in the supercages and sodalite cage, respectively. The third band at 3740 cm^{-1} is assigned to the presence of low- or non-acidic terminal (or external) silanol groups (Si-OH) on the external surface of the zeolite, which are usually present at the termination of the zeolite crystals. It is interesting to note that the band corresponding to the terminal (or external) silanol groups is already quite prominent for the parent HY zeolite, which may be associated with the high amount of mesopores in this sample (Table 1). Since native zeolites are commonly microporous materials, the high mesoporosity of the commercial HY zeolite used in this work might indicate that this material underwent a mesopores generation process, most likely due to a post-synthesis treatment. Mesopores generation by post-synthesis treatment is indeed known to produce silanol groups on the zeolites [38]. In this case, silanol generation seemed to have occurred only on the external surface of the zeolite, as no band assigned to internal silanols (usually at 3720–2710 cm^{-1}) is noticed. It can also be observed that the intensities of both bands at 3565 and 3630 cm^{-1} for the steamed HY zeolite remain pretty much similar to those for the HY zeolite. However, the steamed HY zeolite shows an increased number of silanol groups (Si-OH) in comparison to the parent HY zeolite. This is most likely caused by the development of an additional mesoporosity in the zeolite crystals, which increased the external surface area. As mentioned earlier, silanol groups can be generated via post-synthetic treatments, such as the dealumination by steaming. Normally, removal of aluminium starts to be observed from the external surface of the crystal, being followed by Al-O bond hydrolysis within the T-O-T (T = Si or Al) groups of the zeolite when more severe conditions are used [38]. Under the conditions of this work, only a very mild steam treatment was applied with removal of only EFAL species from the outer surface of the zeolite. This, consequently, led to an increase in the mesoporous volume and external surface area of the HY zeolite, and so to the generation of silanol groups on the external surface (external or terminal silanols). In fact, as soon as extra external surface area is created on a zeolite, silanol groups are required to finish off the surface. Moreover, no bands associated with the generation of additional extra-framework Al species were found for the steamed sample. This is not surprising considering that no framework aluminium was removed during the steaming treatment, as discussed earlier (Table 1). Additional EFAL species would only be generated if framework aluminium removal and retention would have taken place. On the other hand, the addition of Ni to the HY and steamed HY zeolites caused a reduction in the Al-OH-Si groups both located in the supercages and sodalite cages, which might be due to the addition of some Ni^{2+} in exchange positions (i.e., presence
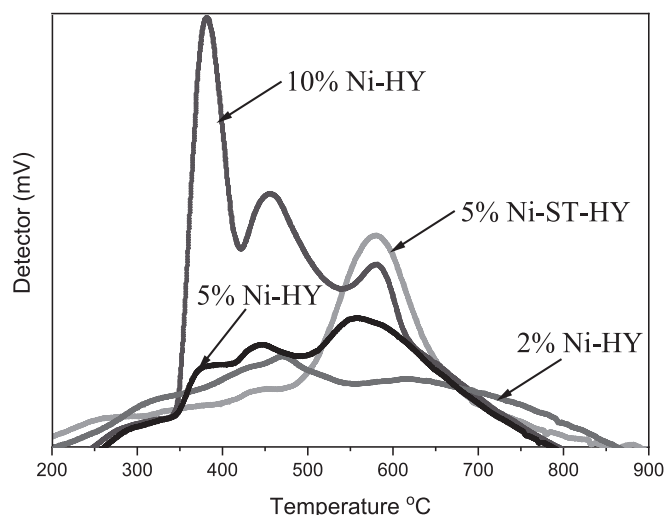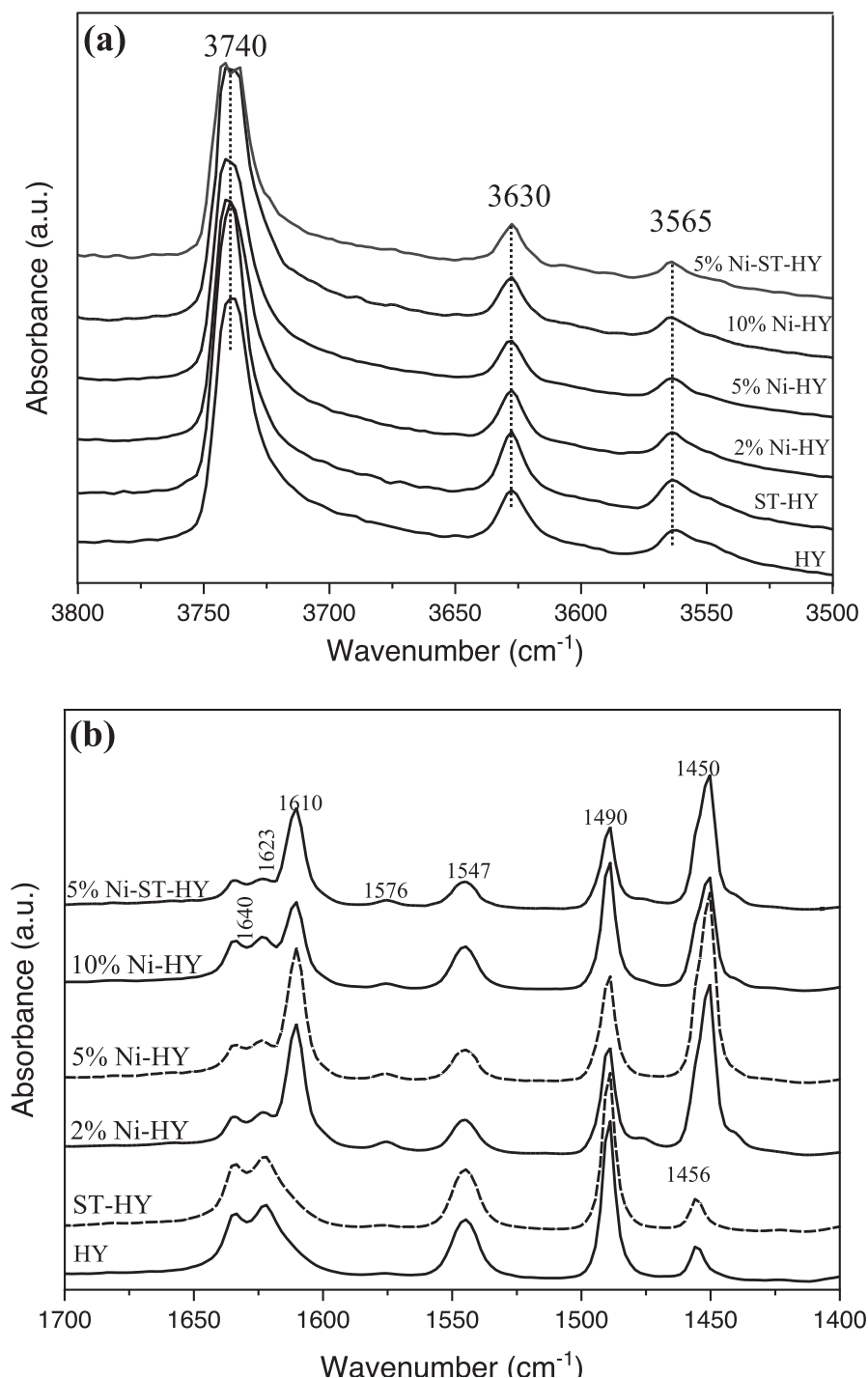

Fig. 3. H_2-TPR profiles of Ni loaded HY and steamed zeolites.

Fig. 5. (a) FTIR spectra in the OH-region (3800–3500 cm^{-1}) before pyridine adsorption and (b) difference spectra after and before pyridine adsorption at 150 ℃ in the 1700–1350 cm^{-1} region, for the HY and its modified samples.

of new Ni^{2+} Lewis acid sites). However, the terminal silanol groups remained practically unaffected.

Fig. 5b displays the difference spectra after and before pyridine adsorption at 150 °C for the parent HY zeolite and its modified samples in the range of 1700–1400 cm^{-1}. The bands at 1455 and 1623 cm^{-1} correspond to coordinatively adsorbed pyridine in the Lewis acid sites (PyL), while the bands at 1547 and 1640 cm^{-1} are assigned to the pyridinium ions (PyH$^+$, interaction with the Brønsted acid sites). The band at 1490 cm^{-1} is ascribed to the interaction of pyridine with both Brønsted and Lewis acid sites. While these bands are the only ones observed for the HY and steamed HY zeolites, the impregnation of the

samples with Ni leads to the appearance of additional very intense bands at 1610 and 1450 cm^{-1}, and a small band at 1575 cm^{-1}. The presence of these bands can be assigned to pyridine coordination to divalent cations, in this case Ni^{2+} [39–41].

The concentrations of Brønsted and Lewis acid sites on the zeolite samples were determined by integrating the bands at 1547 and 1455 cm^{-1}, using 0.9 and 1.58 cm/μmol as extinction coefficients (determined in-house), respectively. The total amount of Brønsted and Lewis acid sites determined by pyridine adsorption at 150 °C are summarized in Table 1. Steaming of the HY zeolite seems to lead to a very slight increase in the Brønsted acid sites concentration. On the other hand, a

little decrease in the concentration of the Lewis acidity can also be seen, which may be due to the removal of some extra-framework Al (EFAL) species during steaming. This could also result in more accessible Brønsted acid sites, explaining the increase in their concentration. These observations are in line with the increase in the microporous volume for the steamed HY zeolite, when compared to the HY zeolite (Table 1). As expected, with the addition of Ni on both the HY and steamed HY zeolites, the concentration of Brønsted acid sites is reduced with a consequent increase in the Lewis acidity [37]. The decrease in the Brønsted acid sites after Ni addition could be due to the interaction of this metal with the bridging hydroxyl groups of the zeolite, which coincides with the observed reduction in the intensity of the bands at 3565 and 3630 cm^{-1} (Fig. 5a) in the presence of Ni. In fact, during impregnation of Ni, some Ni^{2+} ions can exchange with the protons present in the zeolite framework. This incorporation of Ni^{2+} ions in exchange positions together with the impregnated Ni are responsible for an increase in Lewis acidity, which is not surprising since transition metals can induce their generation [37,42]. Interestingly, the reduction in the Brønsted acidity due to the addition of Ni is more important in the case of the steamed HY zeolite than for the HY zeolite, at the same amount of Ni added (5 wt%). This could be due to the fact that the 5%-ST-HY zeolite presents octahedral Ni^{2+} particles in exchange positions rather than just NiO, as observed by UV–Vis spectroscopy (Fig. 4).

Moreover, Fig. S1 depicts the evolution of the concentration of the Brønsted and Lewis acid sites with the increase in the temperature. It can be seen that the evolution of the Brønsted acid sites is similar up to 350 °C for the steamed HY and HY zeolites, while their amount decreases abruptly at 450 °C for the steamed HY zeolite. This shows that the strength of the strongest Brønsted acidity is lower for the steamed HY zeolite than for the HY zeolite, which may be due to the removal of some EFAL species during the steaming treatment. In fact, it is well-known that the interaction of the Brønsted acidity with EFAL species increases the strength of the Brønsted acid sites [43]. After the addition of Ni, although the zeolites did not have the same total amount of Brønsted at 150 °C, the concentrations of this type of acid sites determined at higher temperatures all progressively decrease towards zero. This observation shows that the Ni deposition leads to a decrease in the strength of the Brønsted acidity. Concerning the Lewis acid sites, their strength remains identical up to 350 °C when comparing the steamed HY and HY zeolites, while it is reduced for the steamed HY zeolite when increasing the temperature further. With the Ni impregnation, independently of the amount of Ni, the amount of Lewis acid sites on the samples progressively tends to the same value with the increase in the temperature. Hence, the number of strong Lewis acid sites appears to be similar for all the zeolites. Additionally, it can be concluded that the additional Lewis acidity generated by the presence of the metal appears to be rather weak in nature, as the number of Lewis acid sites able to retain pyridine at 250 °C is already very similar for all the zeolites.

3.2. Surgical face masks characterization

The composition of the waste surgical face masks was analysed using Fourier-transform infrared spectroscopy (FTIR), as illustrated in Fig. 6. Based on the configuration, a set of moderately intense absorption peaks at 810, 844, 996 and 1170 cm^{-1} appeared in the spectra for all the 3-plies of surgical face mask, which are attributed to the absorption bands of isotactic polypropylene [44]. Similarly, the sharp and distinct peaks for all sides of surgical mask at 1378 and 1458 cm^{-1} correlate the –CH$_3$ and –CH$_2$ deformation to the polypropylene polymer, respectively. In addition, C-H stretching bands similar to the polypropylene reference are shown by the strong peaks at 2836, 2916 and 2950 cm^{-1} [10]. In general, these peaks can reveal that all the three plies of surgical face masks are composed of polypropylene (i.e., a thermoplastic) and suggesting that they may be utilized as a feedstock for the hydrocracking process to generate fuels.

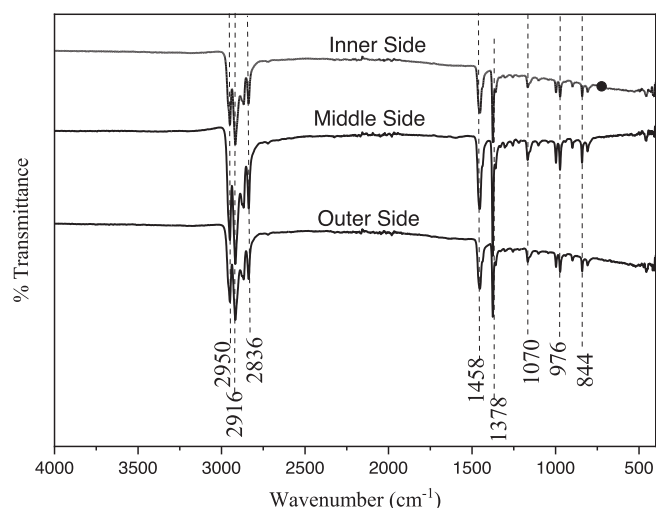Fig S2a illustrates the TGA curve for the degradation of waste

Fig. 6. FTIR spectra of 3-ply waste surgical face mask.

surgical face mask with respect to temperature (°C). The degradation starts at 265 °C (T$_{5\%}$) and 95% of the sample was degraded at 380 °C (T$_{95\%}$). This evidences the significant energy requirements for the cracking of waste surgical face masks into value-added chemicals. Moreover, only one single peak appeared on the DTG curve (Fig. S2b) which confirms the single step degradation of waste surgical face masks.

4. Hydrocracking experiments

4.1. Surgical face masks hydrocracking reactions

Fig. 7 shows the conversions and product selectivities obtained in the presence of the zeolites without and with Ni addition. A conversion of only 26 wt% was obtained after the thermal run at 325 °C, with the main products being gases and solids (blank run without catalyst). However, the addition of a catalyst leads to a significant enhancement of the conversion, which depends on the catalyst added. This clearly shows the benefit in adding a catalyst when performing the hydrocracking of the surgical face masks. Indeed, a conversion of 75.3 wt% was reached when utilizing the commercial Y zeolite (HY) as catalyst. Such a high conversion is not surprising since the chosen commercial zeolite already presents a considerable mesoporosity and external surface area. In this case, together with the gaseous products (selectivity = 39.8 wt%), a noticeable selectivity of total liquid products (oils and heavier oils, 60.4 wt%) were found. In fact, after the initial cracking reactions taking place on the outer surface and mesopores of the zeolite, the products formed can migrate to the interior of the framework and undergo further reactions on the microporosity of the zeolite. In detail, hydrocracking in presence of monofunctional Y zeolite usually proceeds via the classical β-scission mechanism, also known as carbenium ion or bimolecular cracking mechanism, which involves three elementary steps: initiation, propagation, and termination [45]. The initiation step consists in the formation of the first carbenium ions and greatly depends on the nature of the reactant. For olefins, the initiation step proceeds through the attack of the zeolite Brønsted acid sites to the olefins double bound, forming a carbenium ion by direct protonation. While a general agreement exists for the olefins initiation step, for paraffins the carbenium ion formation can take place via (1) abstraction of hydride of the paraffin by an olefin that may be present as a feed impurity or be formed in the hydrocracking process, (2) abstraction of hydride ion by a Lewis acid site and/or (3) direct protonation of the paraffin by the Brønsted acid sites, on a C-H or a C-C bond, with formation of a carbonium ion that can crack via protolytic dehydrogenation or cracking, giving a carbenium ion and H$_2$ or a short paraffin. After the formation of the first carbenium ions, isomerization and cracking (β-scission) reactions of this carbocation
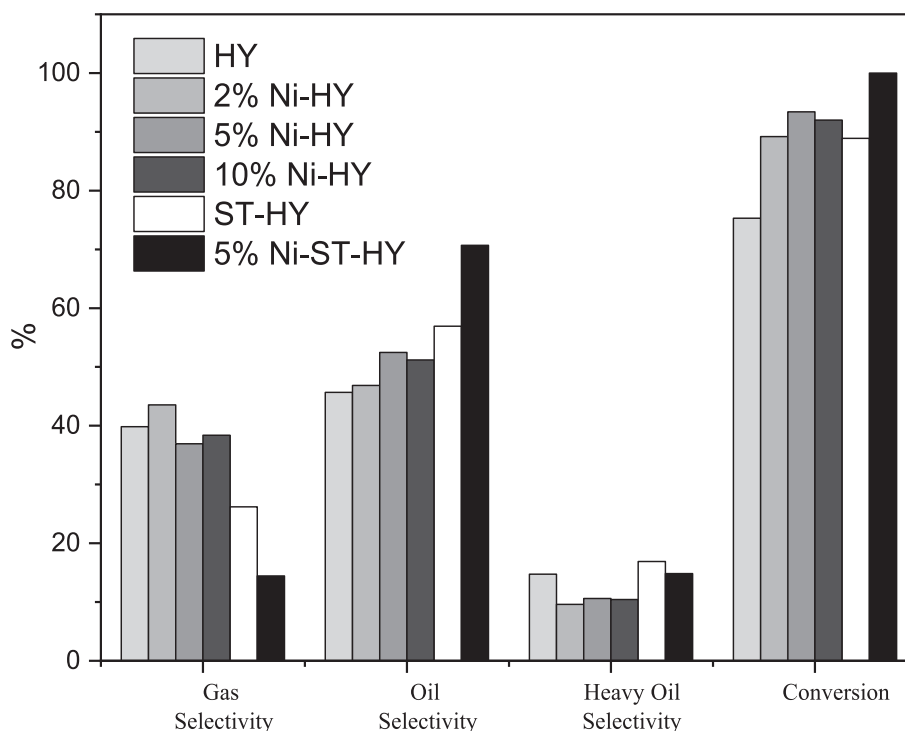
Fig. 7. Product selectivity and conversion of surgical face masks through hydrocracking over HY zeolite with different loading of Ni and steamed HY zeolite with 5 wt% Ni in a 100 mL autoclave reactor, 10 bar initial cold H_2 pressure, feed to catalyst ratio of 10:1 (by weight), 325 ℃ for 120 min residence time.

resulting in smaller carbenium ions and olefins can then occur [46]. The presence of high partial pressure of hydrogen resulted in the hydrogenation of these olefins before they appeared in the final product.

The addition of Ni to the zeolite support is known to be responsible for altering the reaction mechanism, where the feed begins to be dehydrogenated on the Ni sites to obtain olefins (step I). In the second step, these olefinic compounds are isomerized and finally cracked by β-scission, forming smaller olefins, which are subsequently hydrogenated on the metal sites, converting the olefinic compounds into saturated compounds [47,48]. Therefore, a metallic source (Ni) was introduced to the HY zeolite, to assess how the variations in the mechanistic processes may impact the cracking of surgical face masks. Compared to the pristine HY zeolite, all Ni loaded HY samples show enhanced conversion. Addition of 2 wt% of Ni enhanced the conversion to 89.2 wt%. Similarly, a further increase in the loading to 5 wt% increased the conversion to 93.4 wt%. However, a further addition of Ni to 10 wt% led to a reduction in the conversion to 92.0 wt%. This may be attributed to the larger Ni particles found on the 10% Ni-HY, which resulted in the reduction of external surface area and porosity of the 10% Ni-HY as compared to the 2% and 5% Ni-HY. Compared to the pristine HY zeolite, overall, the addition of Ni resulted in an increase in the selectivity to lighter oils and a decrease in the generation of heavier oils. The observed increase in activity and selectivity to lighter oils might be due to the introduction of an additional Lewis acidity by Ni. Despite the reduction in the Brønsted acid sites with the Ni incorporation on the zeolites, the total acidity of the zeolite (Brønsted + Lewis acid sites) increases with the addition of Ni (Table 1). These newly created Lewis acid sites by addition of Ni can indeed also be involved in the initiation of the cracking chain mechanism in two ways: (1) hydride abstraction directly forming the first carbenium ions and (2) formation of olefins by dehydrogenation, which can subsequently be protonated on the Brønsted acid sites and form the first carbenium ions. Therefore, this improvement of the cracking initiation step by Ni can help in the generation of the carbocations for the subsequent cracking reactions, helping in the further cracking of heavier oils during the reaction.

Although the addition of Ni already contributes for the enhancing of

the hydrocracking of the surgical face masks, the use of hierarchical zeolites (i.e., steamed HY zeolite) was also considered for further hydrocracking reactions. Compared to the commercial HY zeolite, the steamed HY zeolite (ST-HY) considerably improved the conversion of surgical face masks from 75.3 to 88.9 wt%. Given that the ST-HY exhibits higher external surface area than the pristine HY zeolite (Table 1), a significant cracking is believed to occur on the external surface of the zeolite, leading to the rapid production of shorter polymeric chains. These smaller polymer molecules coupled with the enhanced porosity of ST-HY, where a higher number of active sites may be reached, result in the reduction in the diffusional restrictions of the molecules inside the zeolite framework. An increase in the selectivity to total liquid products (i.e., 60.4 wt% to 73.8 wt%) and a decrease in the selectivity to gases (i. e., 39.8 wt% to 26.2 wt%) were also observed with the steamed HY zeolite, when compared to the HY zeolite. This can be due to the reduction in the retention time of the molecules inside the steamed HY zeolite structure as a result of the improved diffusion rates combined with the decrease in the strength of the Brønsted acid sites (Fig. S1), which prevent further cracking of the oils into gases. Moreover, addition of 5 wt% of Ni over ST-HY exceptionally increased the conversion to 100 wt%. The combination of the improved diffusion rates with the more uniform dispersion and smaller average in Ni particle size as compared to Ni-loaded HY samples may be at the origin of the observed behaviour. This argument is in accordance with previous literature [49]. In addition, the selectivity to total liquids is considerably higher than for the other catalysts (85.5 wt%), possibly also as a result of the enhanced diffusion.

4.2. Liquid products distribution

Fig. 8a illustrates the selectivity within the oil products range for the various catalysts based on the GC analysis of their n-heptane soluble liquids. HY zeolite and its Ni-loaded samples showed 100 wt% selectivity towards gasoline-range fuels (C_5-C_{12}). In detail, pristine HY zeolite exhibits maximum affinity towards C_9-C_{12} range fuels, while the addition of Ni shifted the trend towards lower boiling point hydrocarbons
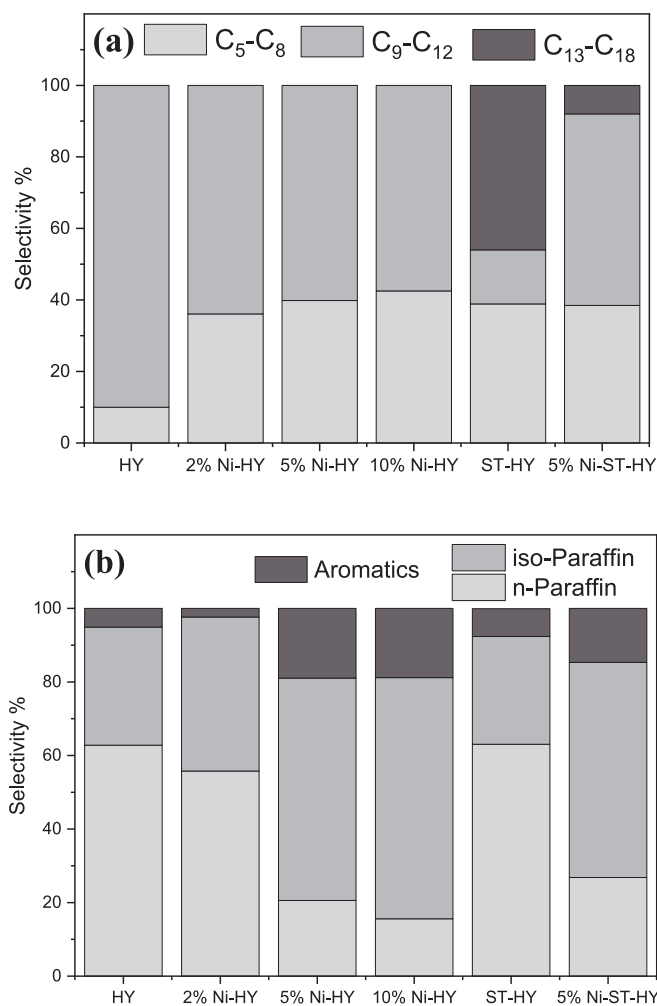
Fig. 8. Selectivity of the n-heptane soluble liquids obtained by the hydrocracking of surgical face masks over various catalysts in a 100 mL autoclave reactor, 10 bar initial cold H_2 pressure, feed to catalyst ratio of 10:1 (by weight), 325 °C for 120 min residence time. (a) Product selectivity based on carbon number, (b) Product selectivity of n-paraffins, *iso*-paraffins and aromatics.

(C_5-C_8), with consequent depletion of C_9-C_{12} products as the reaction begins by a distinct mechanism that favours the cracking reactions. In the case of the steamed HY zeolite, the catalyst shows selectivity towards both gasoline (C_5-C_{12}) and diesel range fuels (C_{13}-C_{18}), due to the lower retention times inside the zeolite structure that reduce the occurrence of chain cracking reactions. However, the addition of Ni remarkably shifted the diesel range fuels to the gasoline range. In fact, the selectivity of C_9-C_{12} increased at the expense of C_{13}-C_{18}, whereas the introduction of Ni has barely any effect on the yield of C_5-C_8. As mentioned before, the addition of Ni leads to a higher preponderance of dehydrogenation reactions, which form olefinic species that more easily form carbocations and lead to the occurrence of cracking, which could explain the lower amount of heavier gasoline-range products. In addition, longer-chain carbocations are much more stable than lower-chain ones, which may result in a higher cracking activity of higher- carbon number hydrocarbons.

Moreover, it is possible to see in Fig. 8b that the HY zeolite led to high n-paraffins in the gasoline-range products with a little selectivity towards aromatics. The introduction of Ni promoted the branching (isomerization) and aromatization ability of the HY zeolite. This can be explained by the fact that isomerization and reactions involved in the aromatization of hydrocarbons (oligomerization, hydrogen transfer,

cyclization) also proceed via a mechanistic chain that requires the formation of carbenium ions as initiating step [45]. It was previously discussed that the addition of Ni creates Lewis acid sites that can further promote the formation of carbenium ions, and so favour all the reactions that require carbenium ions as initiating step [45]. Increase in Ni loading from 2 to 10 wt% notably enhanced the iso- to n-paraffins ratio from 0.75 to 4.20. On the other hand, the aromatization ability of the HY zeolite was maximum at 5% Ni loading and a further increase in Ni did not enhance the aromatic content. Similarly, the presence of Ni over the steamed Y zeolite increased the iso- to n-paraffins ratio from 0.52 to 2.18, whereas the aromatic yields doubled. Therefore, the results show that a suitable selection of the support and Ni amount could direct the hydrocracking of the surgical face masks to the production of gasoline-range only or gasoline- and diesel-range products, according to market demand.

4.3. Reusability of spent catalysts

In a catalysed reaction, understanding of catalyst stability and reusability is an important activity from an economic and technological perspective. To investigate whether the 5% Ni-ST-HY zeolite, the catalyst showing the best results, could be employed in consecutive runs or if a regeneration step would be required, various experiments were performed. Therefore, three consecutive reaction runs without intermediate regeneration were carried out, with the catalyst being recovered, washed and dried after each run to be used in the following one. After the third reaction run, the catalyst was recovered, but this time it was submitted to a regeneration process by calcination under air flow followed by reduction under hydrogen. The same reaction conditions were used in all the reaction runs.

Fig. 9 shows the results of hydrocracking reactions for the three consecutive reaction runs without regeneration and the reaction run where the catalyst was regenerated. It can be observed that a small decrease in the conversion takes place when using the catalyst for three times without regeneration. This reduction in the catalyst activity is more evident when going from the second to the third reaction runs. Indeed, in the first (100 wt%) and second (98.1 wt%) runs almost identical conversions were achieved, whereas in the third run a slightly lower conversion was obtained (91.6 wt%). Even though the conversion does not change massively, this activity decay was accompanied by a very significant increase in the selectivity of gases (from 14.5 wt% to 51.8 wt%) and a decrease in the selectivity of total liquids generated (from 85.5 wt% to 48.2 wt%). This evidences that there is a higher
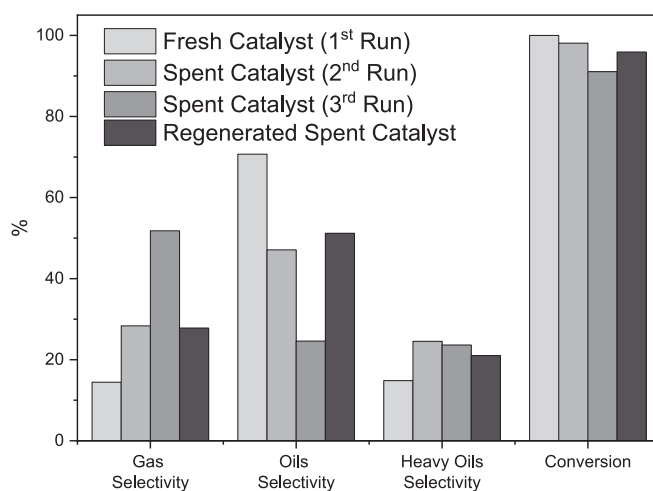
Fig. 9. Product selectivity and conversion of surgical face masks through hydrocracking over fresh, spent and regenerated spent 5% Ni-ST-HY catalyst. 100 mL autoclave reactor, 10 bar initial cold H_2 pressure, feed to catalyst ratio of 10:1 (by weight), 325 °C for 120 min residence time.

preponderance of the thermal cracking relatively to the catalytic cracking due to the deactivation of the catalyst.

To understand the reasons for the observed behaviours of the spent catalyst, the catalysts after the second and/or third reaction runs were analyzed by TGA, N_2 physisorption and TEM. Fig. S3 shows the TGA profiles for the spent 5% Ni-ST-HY catalyst after the second and third reaction runs. Weight losses of 31 and 51 % were observed for the catalysts after the second and third reaction runs respectively. This clearly indicates the presence of carbonaceous materials over the catalysts after the reaction runs, which will most likely be a combination of coke and unreacted plastics. As a result of this carbonaceous materials deposition, the recovered catalyst after the third reaction run showed a significant decrease in its textural properties (Table 1). In addition, TEM analysis of the fresh catalyst and spent catalyst after the third reaction runs (Fig. 2d and e) revealed an increase in the average Ni particle size from 9 to 14 nm, showing that some sintering of the Ni particles took place under the hydrocracking conditions. Therefore, deactivation of the catalyst seems to be due to a combination of coke formation that leads to a partial blockage of the catalyst porosity, and so decreases the access to the active sites, and of sintering of the metal particles.

Moreover, the spent catalyst after the third reaction run was regenerated and utilized for the hydrocracking experiment. Interestingly, the regenerated catalyst showed an enhanced conversion (95.9 wt%), together with an increase in the total liquids selectivity (72.2 wt%) and a decrease in the selectivity of gaseous products (27.8 wt%), when compared to the third reaction run. Values obtained after regeneration are closer to those of the second reaction run. In fact, calcination of spent catalyst (i.e., regenerated spent catalyst) notably enhanced the porosity and external surface area due to the removal of carbonaceous materials from the catalyst (Table 1). It is also possible that some redistribution of the Ni metal particles might have happened as a result of the thermal treatment as confirmed by TEM results (Fig. 2f). Overall, the results suggest a slight decrease in selectivity of the catalyst after being used in cyclic runs. However, the catalyst remains active after an effective regeneration process.

Fig. 10 illustrates the selectivity within the lighter oil fraction extracted from the hydrocracking of surgical mask over the three consecutive reaction runs without regeneration and the reaction run where the catalyst was regenerated. It was found that the fresh Ni-ST-HY catalyst showed maximum selectivity towards gasoline range fuels (C_5-C_{12} = 92.0 wt%), with some affinity towards higher carbon range diesel products (C_{13}-C_{18} = 7.97 wt%). On the other hand, the spent catalyst after the second and third reaction runs showed a decrease in the selectivity for the gasoline range fuels (i.e., 2nd run = 77.6 wt%, 3rd run = 76.2 wt%) with an increase in the selectivity to higher hydrocarbons (C_{13}-C_{18}), as a result of the supressing of the cracking function due to the blockage of the active sites by coke. However, the regenerated spent catalyst showed again a higher selectivity to gasoline range fuels (85.5 wt%) with a decrease in the selectivity to diesel fuels (14.5 wt%), as shown in Fig. 10a. This further cracking of high boiling point hydrocarbons to lower ones over the regenerated spent catalyst may be assigned to the increase in the accessibility of the active sites of the catalyst due to the removal of some of the carbonaceous material by calcination.

In addition, the spent catalyst showed a decrease in selectivity to aromatics and *iso*-paraffins with a significant increase in the selectivity to n-paraffins. Compared to the fresh catalyst (first reaction run), the iso- to n-paraffins ratio of second and third reaction runs of spent catalyst changed from 2.18 to 1.14 and 0.58 respectively (Fig. 10b). This is no strange considering that, with the carbonaceous materials accumulation on the catalyst and the subsequent decrease in the porosity, the diffusion of the aromatics and *iso*-paraffins to the outside of the zeolite structure will be more hindered since these products are more voluminous than the n-paraffins. Regeneration of the spent catalyst significantly enhanced the iso- to n-paraffins ratio. However, there was only a little increase in the yield of aromatics, as these are bulkier than the paraffins.
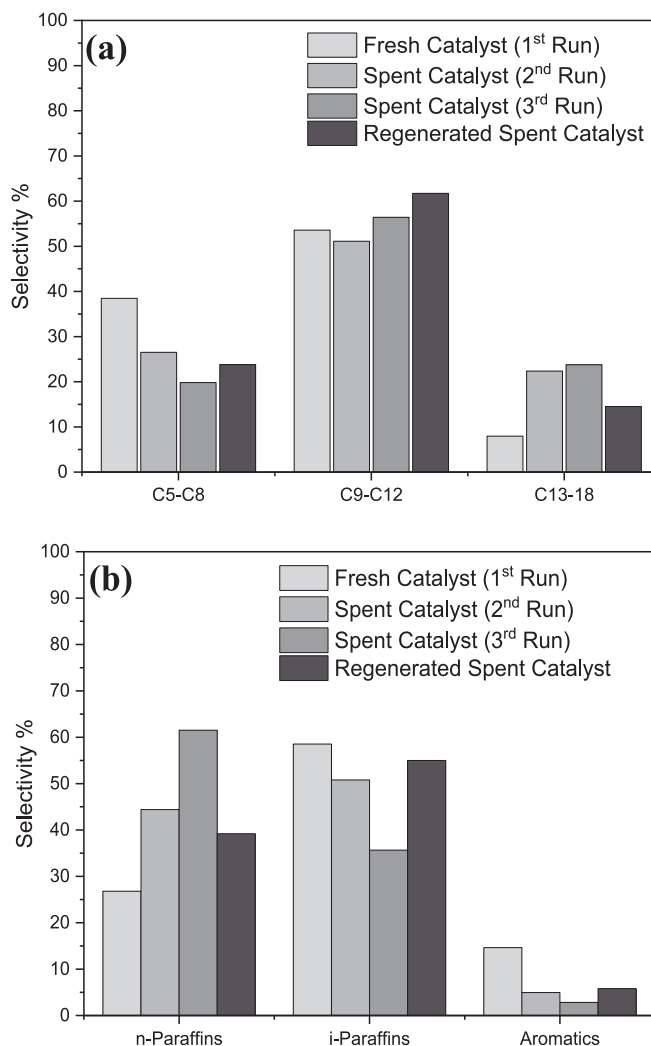
Fig. 10. Selectivity of the n-heptane soluble liquids obtained by the hydrocracking of surgical face masks over fresh, spent and regenerated spent catalyst in a 100 mL autoclave reactor, 10 bar initial cold H_2 pressure, feed to catalyst ratio of 10:1 (by weight), 325 °C for 120 min residence time. (a) Product selectivity based on carbon number, (b) Product selectivity of n-paraffins, *iso*-paraffins and aromatics.

4.4. Comparison with literature

The performance of the Ni loaded hierarchical zeolite (i.e., 5% Ni-ST-HY) for the hydrocracking of surgical face masks was also compared with the recent studies for the pyrolysis of surgical face masks and hydrocracking of polypropylene (Table 2). Recently, Li et al. [11] studied the pyrolysis of waste masks to liquid fuels. Thermal pyrolysis of middle (MLM), inner and outer layers (IOM) of surgical mask was performed at slow and medium modes within a temperature range of 350–650 °C. Mild pyrolysis of both MLM and IOM produced an oil selectivity of 74.6 and 86 wt% whereas gaseous products showed selectivity in the range of 23.8 and 13 wt% respectively at 650 °C. However, due to the elevated temperature requirements, the generation of CO, CO_2 and char along with mild high heating value (HHV) of oily products (i.e., 41 MJ/kg) made the process not the best for the recycling of waste surgical face masks. Aragaw et al., [10] did a similar work, where the pyrolysis of surgical face masks and gloves were carried out at 400 °C for 1 h. Interestingly, the process only showed 75 wt% of liquids selectivity with a significant quantity of char (i.e., 10 wt%). However, the waxy nature of the liquid products (i.e., kerosene) obtained from the pyrolysis of surgical face masks and gloves made it difficult to be utilized directly as

Table 2

Performance comparison of various catalytic hydrocracking and other chemical recycling techniques with current study.

Catalyst	Feed	Process	Reaction Conditions				Selectivity (wt%)			Conv. (wt%)	Ref.
			P_{H2} (bar)	T (℃)	t (min)	F:C[a]	Gas	liquids	Solid		
5% Ni-ST-HY	Surgical face Mask (PP)	Hydrocracking	10	325	120	10:1	14.45	85.54	0	100	Present work
Thermal	Surgical Mask (PP)	Pyrolysis	–	650	30	–	14–23.8	74.6–85	1–1.6	98.4	[11]
Thermal	Face masks & Gloves	Pyrolysis	–	400	60	–	15	75	10	90	[10]
$Pt/WO_3/ZrO_2$ with HY(30)	PP	Hydrocracking	30	250	120	10:1	~10	80	~10	~90	[50]
ZSM-5	PP	Hydrocracking	83	430	60	N.G [b]	8.5	61.2	30.2	69.7	[51]

[a] Feed to catalyst ratio.
[b] Not given.

a fuel. Moreover, no study has been done for the hydrocracking of waste surgical face masks. Therefore, a comparative analysis of current study is made with the hydrocracking of polypropylene (PP) because of the similar physiochemical properties of the feedstock. Recently, Liu et al., [50] studied the hydrocracking of polypropylene at mild conditions of temperature (i.e., 250 °C) using $Pt/WO_3/ZrO_2$ mixed with HY as a catalyst. The degradation of PP resulted in a high selectivity of liquid products with maximum in the gasoline range fuels and a small quantity of gases. However, utilization of high pressure of hydrogen (P_{H2} = 30 bar) makes the process uneconomical with a potential hazard of hydrogen. Also, Ali et al., [51] discussed the hydrocracking of PP using ZSM-5 as a catalyst at 430 °C for 1 h. However, the catalyst showed a low conversion of feedstock with a maximum liquid's selectivity of 61.2 wt% which might be due to the smaller size pores and low mesoporosity of the catalyst, which prevents the diffusion of bulky molecules.

Although a completely direct comparison may not be possible due to the differences in the operating conditions and feedstocks used, it is worth noting that the catalytic performance of the best catalyst used in this study (5% Ni-ST-HY) is comparable or superior to those found in the literature. This is indeed achieved while using less severe operating conditions, i.e., lower hydrogen pressure and temperature, which may make the process economically more attractive.

5. Hydrocracking process simulation

Although a simple comparative analysis based on the experimental results and findings is done in Table 2, a comparative analysis of the different management options based on their potential environment impacts is also essential for a better and clear understanding of the processes. Therefore, a life cycle analysis was also performed. In order to

collect information on the energy and material balances along with product analysis to be utilized as inventory data for the potential environmental impacts of the process in the life cycle assessment, an ASPEN model simulation for the hydrocracking of the surgical face masks was also performed.

Hydrocracking of waste surgical face masks was simulated using the Aspen plus V12.1 (39.0.0.116) software. The process flow diagram which consists of three main steps is shown in Fig. 11. Based on the Aspen Plus resources, Peng-Robinson equation of state was chosen as the property method, as it provides reliable findings for lighter hydrocarbons and gases like hydrogen. The stream class details, model parameters and brief explanations of unit operations are provided in Table S1 in Supporting Information. Based on the FTIR analysis (Fig. 6), conventional polypropylene was considered as the substitute material to waste surgical face masks. In the first step, the polypropylene at a mass flow rate of 1 kg.h^{-1} and room temperature (i.e., 20 °C) was mixed with hydrogen with a mass flow rate of 0.010 kg.h^{-1} and at 10 bar. The hydrocracking reaction involves the simultaneous addition of hydrogen and the breaking of carbon–carbon bonds. However, accurate reaction kinetics are difficult to establish because of the uncertainty of the products generated. As a result, a RYield was utilized. The mixed feed was then entered into the reactor (RYield) where decomposition of plastic was done at 325 °C to generate products based on the experimental results. The reactor was assumed to be entirely adiabatic, with all the feed reacted and the process was simplified by modelling it at steady-state. The products from the reactor (R-outlet) were then separated and condensed by installing a series of flash drums (S-1, S-2, S-3, and S-4) and coolers (C-1, C-2 and C-3). The liquid products (LP) were separated as the bottom product after each flash drum, whereas the gaseous products were collected at the end. The utilities for the hydrocracking
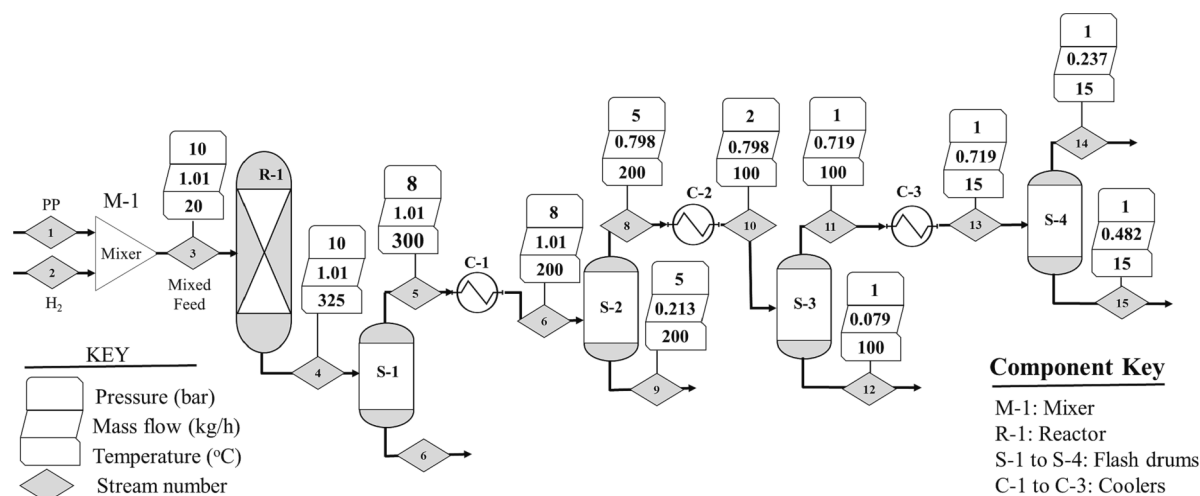
Fig. 11. Process flow diagram of the hydrocracking process model.

process were taken from Aspen database and expressed in terms of heating and cooling duty. Table S2 (Supporting Information) illustrates the utility data of hydrocracking which was further utilized to develop the life cycle assessment.

Moreover, the ASPEN model was validated based on the overall mass and energy balance of the system. Table S3 (Supporting Information) shows the material balance for the whole process (i.e., from mixer to collection of value-added products after separators). Both experimental as well as simulation results showed no solid residual formation during the process. Therefore, whatever it comes from the reactor (R-outlet), it is separated during a series of separators. Based on the product distribution during hydrocracking simulation, liquid and gaseous produced showed results similar to those of the experimental work. Similarly, the obtained products showed an overall heating value of 43.34 MJ.kg^{-1}. Moreover, the model was also validated based on the overall energy balance of the system.

$$Net\ duty = Enthalpy\ of\ feed - Ethalpy\ of\ products + heat\ duty\ of\ equipments \tag{8}$$

$$Enthalpy\ of\ feed = -1.215 kW \tag{9}$$

$$Enthalpy\ of\ Products = -0.083 - 0.027 - 0.223 - 0.231 = -0.564 kW \tag{10}$$

$$Heat\ duty\ of\ the\ equipments = 0.295 + 0.086 + 0.062 + 0.077 = 0.520 kW \tag{11}$$

$$Net\ Duty = -1.215 - (-0.564) + 0.520 \approx 0 \tag{12}$$

The overall heat duty of the system is approximately zero. Therefore, the energy is balanced and validated, and based on this the simulated model was then employed for further analysis.

6. Life cycle assessment

6.1. Goal and scope

Herein, life cycle assessment (LCA) is conducted to assess the likely environmental impacts of different waste plastics options. LCA is done by ISO standards and systems. The objective of this study is to estimate the environmental profiles of the management of waste surgical face masks. Different management scenarios i.e., incineration and pyrolysis were compared with hydrocracking of waste surgical face masks with a functional unit of 1 kg of feed. The geographical setting of this LCA was set in the United Kingdom (UK). Moreover, the definition of the system boundary is one of the essential concerns of the LCA study, as it decides what unit processes to be excluded and what to be involved in investigation. Fig. 12 illustrates the system boundary for life cycle assessment for all the three scenarios from gate to grave i.e., after transportation of feed to end of life. In detail, waste surgical face masks undergo one of the three different waste management scenarios: (I) incineration with energy recovery i.e., WtE (100%), (II) pyrolysis or (III) hydrocracking. Moreover, the following assumptions were modelled in this LCA study: (i) all the management facilities considered in this study were supposed to be at same location and impact of waste transportation is similar for all scenarios. Similarly, impact of transportation within the facility was also considered negligible and therefore out of the scope of this study; (ii) steam generated during incineration was only utilized for electricity production; (iii) synthesis of catalyst has no environmental impact, therefore was not considered in the LCA; (iv) based on the polymeric nature of surgical face masks, LCA of PP was considered when and where required; and (v) only three layers of waste surgical face masks were considered for the life cycle analysis.

6.2. Life cycle inventories for current scenarios

Life cycle inventory management is ultimately the most complex step of LCA, as it requires to accumulate, measure, and investigate data on basis of inputs and outputs during LCA. In this study, inventory data was collected from various literatures for different management scenarios.
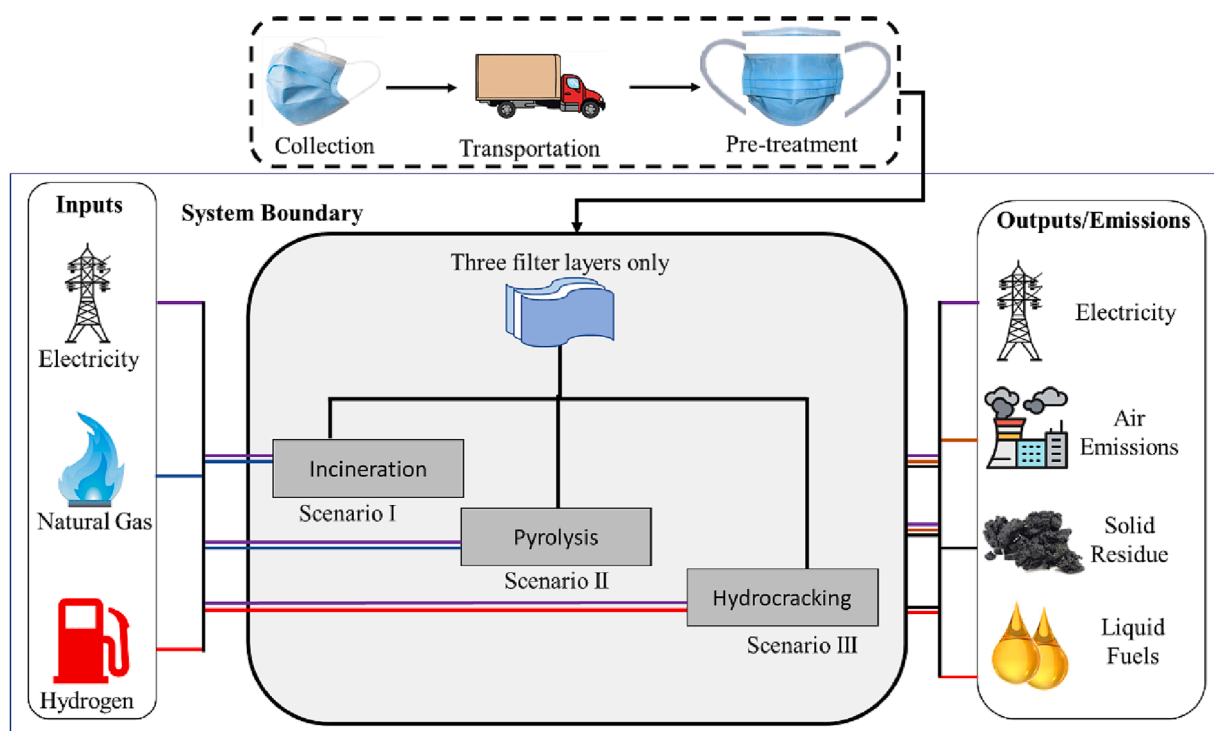

Fig. 12. Life cycle scenarios, system boundary and various LCA scenarios for the management of waste surgical face masks.

Ecoinvent database in SimaPro software was used to analyze missing data. Waste to energy process inventory data were extracted from past studies [6,52] and compiled in Table S4 (Supporting Information). Moreover, inventory data for the pyrolysis of waste surgical face masks were referred from a recent study of Li et al. [11] and presented in Table S5 (Supporting Information). In addition, inventory data for the hydrocracking process were based on experimental results and missing information was taken from previous studies [53]. Based on the author's assumptions, only pyrolysis oil was utilized as a desired product and employed to generate electricity of 3.2 kWh. However, considering the management scenarios in the UK, the pyrolysis oil was supposed to be combusted to produce electricity (i.e., electricity, high voltage {GB}, Great Britain data). Similarly, the outputs of both incineration and pyrolysis resulted in the energy generation (i.e., electricity). Therefore, for a better comparison of the results, it was considered that liquid fuels and gaseous products obtained from the hydrocracking of waste surgical face masks were utilized for electricity production (3.85 kWh). The value was calculated based on the calorific value of products obtained from process simulation and literature [54]. The data for production of resources needed (e.g., electricity) were obtained directly from Ecoinvent 3 database. Moreover, information related to Great Britain {GB} was utilized when accessible.

6.3. Life cycle impact assessment (LCIA)

Life cycle impact assessment was completed utilizing SimaPro 8.3.0 software and by adopting CML-IA baseline V3.0.4 world 2000 methodology. The CML-IA baseline is a problem-oriented and midpoint approach which reduces the uncertainty in life cycle impact assessment mechanism. Moreover, it also connects all phases of inventories by means of different impact category and universally applies for potential environmental impacts assessment. However, the current study just discussed and explained the six most studied and discussed impact categories which are expressed in Table 3 below.

6.4. LCA results and discussion

The overall LCIA midpoint characterization results for the management of waste surgical face masks based on three different scenarios for various impact categories using CML-IA baseline method are illustrated in Table 3. Similarly, a detailed comparative environmental impact assessment of waste surgical face masks with various management scenarios is illustrated in Table S7 (Supporting Information). Overall, scenario III (i.e., hydrocracking) showed the least environmental impacts on six impact categories, while scenario I (i.e., incineration) displayed the worst scenario for the waste surgical face masks management. The overall discussion of potential of each scenario with individual waste management option considered is further explained below.

Table 3
Environmental impacts for the management of waste **surgical** face masks on various impact categories.

Impact category	Unit	Incineration	Pyrolysis	Hydrocracking
Abiotic depletion	kg Sb eq	2.65×10^{-07}	-6.4×10^{-08}	-8.4×10^{-08}
Abiotic depletion (fossil fuels)	MJ	71.99	49.83	48.77
Global warming (GWP100a)	kg CO_2 eq	4.42	0.39	0.17
Ozone layer depletion (ODP)	kg CFC-11 eq	1.65×10^{-08}	-9×10^{-08}	-9.93×10^{-08}
Marine aquatic ecotoxicity	kg 1,4-DB eq	453.41	-1732.38	-1913.49
Terrestrial ecotoxicity	kg 1,4-DB eq	3.69×10^{-4}	-1.72×10^{-3}	-1.88×10^{-3}

6.4.1. Depletion of abiotic resources

Depletion of abiotic resources was grouped in two impact categories: Abiotic depletion (elements) and Abiotic depletion (fossil fuels). The first one describes the extraction of abiotic (i.e., Non-Living) assets such as minerals, resources and is quantified in kilograms of antimony equivalents (kg Sb eq.), while the latter refers to the consumption of energy content of fossil fuels and is measured in megajoule (MJ). Environmental impact assessment of all three plastic waste management scenarios on Depletion of Abiotic resources is demonstrated in Fig. S4a. Overall, both pyrolysis and hydrocracking scenarios showed positive impact with negative values on abiotic depletion, whereas incineration showed a negative impact. In detail, management of waste surgical face masks using incineration process utilizes both electricity and natural gas as resources and significantly produces a range of gaseous products with only a limited quantity of electricity produced. This in general produces an overall negative impact on environment. On the other hand, a notable generation of electricity during pyrolysis creates an overall positive impact on abiotic depletion. Moreover, during hydrocracking utilization of hydrogen, electricity and cracking of waste surgical face masks impacted negatively on abiotic depletion. However, generation of electricity made an overall positive impact (-8.4×10^{-08} kg Sb eq.). Similarly, Fig. S4b illustrates the impacts on abiotic depletion (fossil fuels) for all scenarios and displays the total opposite trend as seen in abiotic depletion (elements). All management options demonstrated a positive value due to utilization of energy content of waste plastics and utilities. Based on the results, it can be concluded that hydrocracking is the only scenario which utilized the most of waste resource to create minimum impact on abiotic depletion (fossil fuels 48.77 MJ). To conclude, scenario III displayed the least impacts on abiotic depletion, whereas incineration highlighted the worst scenario for overall abiotic depletion of minerals and fossil fuels.

6.4.2. Climate change

Impact of climate change is investigated in terms of greenhouse gases (GHG) emissions to air which have adverse impact on environment and cause global warming. The impact of this global warming is measured in terms of the mass of CO_2 per kg of GHG's for a time span of one hundred years (GWP100a). Fig. 13 summarizes the effect of all scenarios on global warming (GWP100a) impact category. Overall, scenarios I and II revealed a negative impact while scenarios III presented the most favourable scenario. In detail, scenario I showed maximum impact (4.42 kg CO_2 eq./FU) due to substantial number of emissions (e.g., GHGs) during incineration process. Similarly, consumption of electricity and natural gas along with burning of valuable resource (i.e., waste
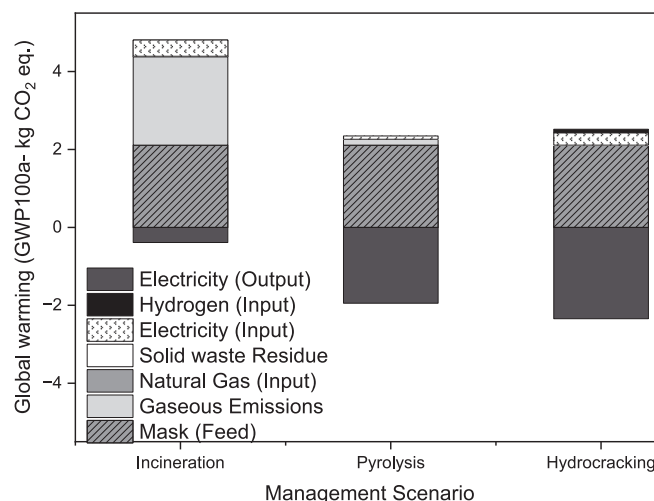
Fig. 13. Impact assessment of waste surgical face masks management scenarios on global warming GWP100a (kg CO_2 eq.).

surgical face masks) significantly generate a large amount of CO_2. On the other hand, pyrolysis produces a lower quantity of CO_2 eq. due to the lower consumption of electricity and natural gas during the process and because of the little generation of GHGs during waste management. However, scenario III demonstrated to be the best scenario regarding least impact on global warming (0.17 kg CO_2 eq.) due to the lowest emissions and with maximum utilization of resources for the production of electricity, which ultimately helps to avoid the global warming potential.

6.4.2.1. Ozone layer depletion. Ozone layer depletion compares the proportion of harm a compound can cause to the ozone layer with a comparable mass of trichlorofluoromethane (CFC-11). Results of the present study on ozone layer depletion considering all the scenarios are shown in Fig. S5. It was observed that scenario III showed the least impact on ozone layer depletion because of the maximum amount of energy replacement (i.e., electricity) as an avoided product during the process, which otherwise would deplete ozone layer. Overall, scenario I displayed positive impact with maximum value of 1.65×10^{-08} kg CFC-11 eq.

6.4.2.2. Ecotoxicity. Ecotoxicity refers to the study of ecotoxicology which is the study of potential impact caused mostly by human activities on biota. Through this impact group, the concentration (i.e., measured in 1,4 dichlorobenzene eq.) and type of toxins that cause harm to both plants and animals can be determined. Ecotoxicity can be grouped into several impact categories, but in this study only marine aquatic ecotoxicity (MAE) and terrestrial ecotoxicity (TET) were discussed in detail. The first one (MAE) refers to the effect of toxic chemicals (i.e., released in air, water, or soil) on marine aquatic ecosystem, whereas the TET refers to the impact on land-based animals and their ecosystem. Fig. S6a shows the comparative results of all three scenarios on MAE in 1,4-DB eq. Both pyrolysis and hydrocracking showed positive impact (i.e., negative values) on marine aquatic ecosystem because of the production of electricity as avoided products. However, hydrocracking scenario revealed to be the best scenario based on the maximum utilization of fuels for energy generation which otherwise would create a negative impact on environment. Also, both incineration and pyrolysis scenarios utilized natural gas which subsequently are the potential source of toxicity on marine aquatic ecosystem.

Similarly, the same trend of results was seen for TET in which scenario III (i.e., hydrocracking) showed the least impact on land dependent organisms, whereas incineration is the least preferable scenario as shown in Fig. S6b. Overall, three scenarios showed the following trend in terms of least impacts on ecotoxicity: Scenario III < Scenario II < Scenario I.

To conclude, the conversion of waste surgical face masks by hydrocracking was found to perform better than linear end of life (i.e., incineration) and other circular end of life (i.e., pyrolysis) waste management options. Overall, hydrocracking acquired maximum credits by avoiding the detrimental environmental effects on all six impact categories as compared to pyrolysis and incineration. Therefore, it has been verified that upcycling of waste surgical face masks into value-added energy products is a viable and promising strategy with favourable environmental outcomes.

7. Conclusion

In this work, the hydrocracking of waste surgical face masks, made of polypropylene, was investigated at 325° C and 10 bar initial cold H_2 pressure, over pristine and Ni-loaded HY zeolites. A hierarchical HY zeolite was also synthesized via controlled steaming and modified through Ni addition for the hydrocracking experiments. The characterization results confirmed the formation of mesoporosity with enhanced external surface area as a result of the steaming process. Although the

addition of Ni to the zeolites led to a reduction in the textural properties, it also conducted to the generation of an important number of additional Lewis acid sites. Moreover, steaming of the HY zeolite resulted in the formation of smaller and better dispersed Ni particles, mainly located within the zeolite structure.

For the hydrocracking experiments, addition of Ni to the HY zeolite significantly improved conversion of the surgical face masks due to the enhanced Lewis acidity. Similarly, upcycling of waste surgical face masks over the steamed HY zeolite showed an increase in the conversion with a high selectivity towards liquids and a subsequent decrease in the selectivity to gases. This was most likely due to the higher external surface area and mesoporosity of the zeolite, which resulted in the reduction of the diffusion of the molecules inside the zeolite framework. As expected, Ni-loaded steamed HY zeolite further enhanced the conversion to 100 wt% with an overall selectivity to liquids of 85.5 wt%. These improvements in activity and selectivity were due to the combined effect of improved diffusion rates and dehydrogenation role of Ni, being similar or superior to those reported in the literature. The reusability tests to the 5% Ni-ST-HY revealed that the activity of the catalyst is only slightly affected by coke deposition and sintering of the Ni particles. However, activity could be almost completely restored after the regeneration of the spent catalyst by calcination at high temperature, which removed the carbonaceous materials and led to a redistribution of the Ni particles.

Moreover, a hydrocracking process simulation model was developed based on the experimental data and reaction conditions. Overall, gaseous and liquid products obtained during the process showed an overall heating value of 43.34 MJ.kg^{-1}. The energy inputs (i.e., utility) and product outputs data were extracted to develop a life cycle inventory. A comparative LCA of the surgical face masks showed the benefits of hydrocracking over other linear and circular end of life management options. The current scenario had least impact on abiotic depletion, GWP 100a, ODP, MAE and TET as compared to incineration and pyrolysis. Therefore, this approach and discovery might spark a lot of interest in finding new applications for the upcycling of similar waste.

CRediT authorship contribution statement

Muhammad Usman Azam: Conceptualization, Formal analysis, Investigation, Writing – original draft. **Auguste Fernandes:** Writing – review & editing, Investigation, Formal analysis. **Inês Graça:** Writing – review & editing, Supervision, Resources, Conceptualization. **Waheed Afzal:** Writing – review & editing, Supervision, Resources, Conceptualization.

Declaration of Competing Interest

The authors declare the following financial interests/personal relationships which may be considered as potential competing interests: Muhammad Usman Azam reports financial support was provided by Leverhulme Trust. Auguste Fernandes reports financial support was provided by Portuguese Foundation for Science and Technology.

Data availability

All data has been shared in the main manuscript and as supporting information.

Acknowledgement

00100/2020 and UIDP/00100/2020; IMS - LA/P/0056/2020; contract hiring under DL57/2016 law).

Appendix A. Supplementary data

Supplementary data to this article can be found online at https://doi.org/10.1016/j.fuel.2023.128704.

References

[1] Rosenboom JG, Langer R, Traverso G. Bioplastics for a circular economy. Nature Reviews Materials 2022 7:2 2022;7:117–37. https://doi.org/10.1038/s41578-021-00407-8.

[2] 1.6 Billion Disposable Masks Entered Our Oceans in 2020 n.d. https://www.visualcapitalist.com/1-6-billion-disposable-masks-entered-our-oceans-in-2020/ (accessed December 11, 2022).

[3] Patrício Silva AL, Prata JC, Walker TR, Duarte AC, Ouyang W, Barcelò D, et al. Increased plastic pollution due to COVID-19 pandemic: Challenges and recommendations. Chem Eng J 2021;405:126683.

[4] Chen H, Li J, Li T, Xu G, Jin Xi, Wang M, et al. Performance assessment of a novel medical-waste-to-energy design based on plasma gasification and integrated with a municipal solid waste incineration plant. Energy 2022;245:123156.

[5] van Fan Y, Jiang P, Hemzal M, Klemeš JJ. An update of COVID-19 influence on waste management. Sci Total Environ 2021;754:142014. https://doi.org/10.1016/J.SCITOTENV.2020.142014.

[6] Khoo HH. LCA of plastic waste recovery into recycled materials, energy and fuels in Singapore. Resour Conserv Recycl 2019;145:67–77. https://doi.org/10.1016/J.RESCONREC.2019.02.010.

[7] Purnomo CW, Kurniawan W, Aziz M. Technological review on thermochemical conversion of COVID-19-related medical wastes. Resour Conserv Recycl 2021;167:105429. https://doi.org/10.1016/J.RESCONREC.2021.105429.

[8] Azam MU, Vete A, Afzal W. Process Simulation and Life Cycle Assessment of Waste Plastics: A Comparison of Pyrolysis and Hydrocracking. Molecules 2022, Vol 27, Page 8084 2022;27:8084. https://doi.org/10.3390/MOLECULES27228084.

[9] Chalermsinsuwan B, Li YH, Manatura K. Optimization of gasification process parameters for COVID-19 medical masks using response surface methodology. Alex Eng J 2023;62:335–47. https://doi.org/10.1016/J.AEJ.2022.07.037.

[10] Aragaw TA, Mekonnen BA. Current plastics pollution threats due to COVID-19 and its possible mitigation techniques: a waste-to-energy conversion via Pyrolysis. Environmental Systems Research 2021 10:1 2021;10:1–11. https://doi.org/10.1186/S40068-020-00217-X.

[11] Li C, Yuan X, Sun Z, Suvarna M, Hu X, Wang X, et al. Pyrolysis of waste surgical masks into liquid fuel and its life-cycle assessment. Bioresour Technol 2022;346:126582.

[12] Miranda M, Cabrita I, Pinto F, Gulyurtlu I. Mixtures of rubber tyre and plastic wastes pyrolysis: A kinetic study. Energy 2013;58:270–82. https://doi.org/10.1016/J.ENERGY.2013.06.033.

[13] Munir D, Irfan MF, Usman MR. Hydrocracking of virgin and waste plastics: A detailed review. Renew Sustain Energy Rev 2018;90:490–515. https://doi.org/10.1016/j.rser.2018.03.034.

[14] Ostroumova VA, Severina VA, Maksimov AL. Application of Ni-W Sulfide Catalysts Prepared In Situ from Embryonic and Highly Crystalline ZSM-5 Zeolites in Hydrocracking Reaction of 1-Methylnaphthalene. Pet Chem 2021;61:341–9. https://doi.org/10.1134/S0965544121030191.

[15] Costa CS, Muñoz M, Ribeiro MR, Silva JM. H-USY and H-ZSM-5 zeolites as catalysts for HDPE conversion under a hydrogen reductive atmosphere. Sustain Energy Fuels 2021;5:1134–47. https://doi.org/10.1039/d0se01584a.

[16] Costa CS, Muñoz M, Ribeiro MR, Silva JM. A thermogravimetric study of HDPE conversion under a reductive atmosphere. Catal Today 2021;379:192–204. https://doi.org/10.1016/J.CATTOD.2020.07.021.

[17] Jumah AB, Tedstone AA, Garforth AA. Hydrocracking of virgin and post-consumer polymers. Microporous Mesoporous Mater 2021;315:110912.

[18] Utami M, Wijaya K, Trisunaryanti W. Pt-promoted sulfated zirconia as catalyst for hydrocracking of LDPE plastic waste into liquid fuels. Mater Chem Phys 2018;213:548–55. https://doi.org/10.1016/j.matchemphys.2018.03.055.

[19] Pyra K, Tarach KA, Śrębowata A, Melián-Cabrera I, Góra-Marek K. Pd-modified beta zeolite for modulated hydro-cracking of low-density polyethylene into a paraffinic-rich hydrocarbon fuel. Appl Catal B 2020;277:119070. https://doi.org/10.1016/j.apcatb.2020.119070.

[20] Muñoz M, Morales I, Costa CS, Multigner M, de la Presa P, Alonso JM, et al. Local induction heating capabilities of zeolites charged with metal and oxide mnps for application in hdpe hydrocracking: A proof of concept. Materials 2021;14(4):1029.

[21] Ochoa R, van Woert H, Lee WH, Subramanian R, Kugler E, Eklund PC. Catalytic degradation of medium density polyethylene over silica-alumina supports. Fuel Process Technol 1996;49:119–36. https://doi.org/10.1016/S0378-3820(96)01055-7.

[22] Figueiredo AL, Araujo AS, Linares M, Peral Á, García RA, Serrano DP, et al. Catalytic cracking of LDPE over nanocrystalline HZSM-5 zeolite prepared by seed-assisted synthesis from an organic-template-free system. J Anal Appl Pyrolysis 2016;117:132–40.

[23] Silva BJB, Sousa LV, Sarmento LRA, Alencar SL, Quintela PHL, Silva AOS. Kinetic study of thermocatalytic degradation of UHMWPE over microporous and hierarchical ZSM-23 zeolite. Appl Catal B 2020;267:118699.

[24] Pérez-Ramírez J, Christensen CH, Egeblad K, Christensen CH, Groen JC. Hierarchical zeolites: Enhanced utilisation of microporous crystals in catalysis by advances in materials design. Chem Soc Rev 2008;37:2530–42. https://doi.org/10.1039/b809030k.

[25] Chen L-H, Li X-Y, Rooke JC, Zhang Y-H, Yang X-Y, Tang Yi, et al. Hierarchically structured zeolites: Synthesis, mass transport properties and applications. Article in Journal of Materials Chemistry 2012;22(34):17381.

[26] Weitkamp J. Zeolites and catalysis Solid State Ion 2000;131:175–88. https://doi.org/10.1016/S0167-2738(00)00632-9.

[27] Chen LH, Sun MH, Wang Z, Yang W, Xie Z, Su BL. Hierarchically structured zeolites: From design to application. Chem Rev 2020;120:11194–294. https://doi.org/10.1021/acs.chemrev.0c00016.

[28] Kung HH, Williams BA, Babitz SM, Miller JT, Haag WO, Snurr RQ. Enhanced hydrocarbon cracking activity of Y zeolites. Top Catal 2000;10:59–64. https://doi.org/10.1023/A:1019155832086/METRICS.

[29] Masuda T, Fujikata Y, Mukai SR, Hashimoto K. Changes in catalytic activity of MFI-type zeolites caused by dealumination in a steam atmosphere. Appl Catal A Gen 1998;172:73–83. https://doi.org/10.1016/S0926-860X(98)00120-3.

[30] Pham TN, Nguyen V, Wang B, White JL, Crossley S. Quantifying the Influence of Water on the Mobility of Aluminum Species and Their Effects on Alkane Cracking in Zeolites. ACS Catal 2021;11:6982–94. https://doi.org/10.1021/ACSCATAL.1C01138/ASSET/IMAGES/LARGE/CS1C01138_0010.JPEG.

[31] Lutz W. Zeolite Y: Synthesis, Modification, and Properties-A. Case Revisited 2014;2014:1–20.

[32] Gary JH. Petroleum Refining. Encyclopedia Phys Sci Technol 2003:741–61. https://doi.org/10.1016/B0-12-227410-5/00556-1.

[33] Database of Zeolite Structures n.d. http://www.iza-structure.org/databases/ (accessed April 26, 2022).

[34] Yao D, Yang H, Chen H, Williams PT. Investigation of nickel-impregnated zeolite catalysts for hydrogen/syngas production from the catalytic reforming of waste polyethylene. Appl Catal B 2018;227:477–87. https://doi.org/10.1016/J.APCATB.2018.01.050.

[35] Bai R, Song Y, Li Y, Yu J. Creating Hierarchical Pores in Zeolite Catalysts. Trends Chem 2019;1:601–11. https://doi.org/10.1016/J.TRECHM.2019.05.010.

[36] Graça I, González LV, Bacariza MC, Fernandes A, Henriques C, Lopes JM, et al. CO2 hydrogenation into CH4 on NiHNaUSY zeolites. Appl Catal B 2014;147:101–10.

[37] Gerards RTJ, Fernandes A, Graça I, Ribeiro MF. Towards understanding of phenolic compounds impact on Ni- and V-USY zeolites during bio-oils co-processing in FCC units. Fuel 2020;260:116372. https://doi.org/10.1016/J.FUEL.2019.116372.

[38] Medeiros-Costa IC, Dib E, Nesterenko N, Dath JP, Gilson JP, Mintova S. Silanol defect engineering and healing in zeolites: opportunities to fine-tune their properties and performances. Chem Soc Rev 2021;50:11156–79. https://doi.org/10.1039/D1CS00395J.

[39] Peron DV, Zholobenko VL, de la Rocha MR, Oberson de Souza M, Feris LA, Marcilio NR, et al. Nickel–zeolite composite catalysts with metal nanoparticles selectively encapsulated in the zeolite micropores. J Mater Sci 2019;54:5399–411. https://doi.org/10.1007/S10853-018-03250-5/FIGURES/6.

[40] Graça I, Bacariza MC, Fernandes A, Chadwick D. Desilicated NaY zeolites impregnated with magnesium as catalysts for glucose isomerisation into fructose. Appl Catal B 2018;224:660–70. https://doi.org/10.1016/J.APCATB.2017.11.009.

[41] Penkova A, Bobadilla LF, Romero-Sarria F, Centeno MA, Odriozola JA. Pyridine adsorption on NiSn/MgO–Al2O3: An FTIR spectroscopic study of surface acidity. Appl Surf Sci 2014;317:241–51. https://doi.org/10.1016/J.APSUSC.2014.08.093.

[42] Tao Y, Kanoh H, Abrams L, Kaneko K. Mesopore-modified zeolites: Preparation, characterization, and applications. Chem Rev 2006;106:896–910. https://doi.org/10.1021/CR040204O/ASSET/IMAGES/LARGE/CR040204OF00018.JPEG.

[43] Mezari B, Magusin PCMM, Almutairi SMT, Pidko EA, Hensen EJM. Nature of enhanced brønsted acidity induced by extraframework aluminum in an ultrastabilized faujasite zeolite: An in situ NMR study. J Phy CHem C 2021;125:9050–9. https://doi.org/10.1021/ACS.JPCC.1C00356/ASSET/IMAGES/LARGE/JP1C00356_0012.JPEG.

[44] Hu X, Lin Z. Transforming waste polypropylene face masks into S-doped porous carbon as the cathode electrode for supercapacitors. Ionics (Kiel) 2021;27:2169–79. https://doi.org/10.1007/S11581-021-03949-7.

[45] Pyra K, Tarach KA, Śrębowata A, Melián-Cabrera I, Góra-Marek K. Pd-modified beta zeolite for modulated hydro-cracking of low-density polyethylene into a paraffinic-rich hydrocarbon fuel. Appl Catal B 2020:277. https://doi.org/10.1016/J.APCATB.2020.119070.

[46] Marcilla A, Beltrán MI, Navarro R. Thermal and catalytic pyrolysis of polyethylene over HZSM5 and HUSY zeolites in a batch reactor under dynamic conditions. Appl Catal B 2009;86:78–86. https://doi.org/10.1016/J.APCATB.2008.07.026.

[47] Weitkamp J. Catalytic Hydrocracking—Mechanisms and Versatility of the Process. ChemCatChem 2012;4:292–306. https://doi.org/10.1002/CCTC.201100315.

[48] Mendes PSF, Silva JM, Ribeiro MF, Bouchy C, Daudin A. Quantification of the available acid sites in the hydrocracking of nitrogen-containing feedstocks over USY shaped NiMo-catalysts. J Ind Eng Chem 2019;71:167–76. https://doi.org/10.1016/J.JIEC.2018.11.019.

[49] Escola JM, Serrano DP, Aguado J, Briones L. Hydroreforming of the LDPE Thermal Cracking Oil over Hierarchical Ni/Beta Catalysts with Different Ni Particle Size Distributions. Ind Eng Chem Res 2015;54(26):6660–8.

[50] Liu S, Kots PA, Vance BC, Danielson A, Vlachos DG. Plastic waste to fuels by hydrocracking at mild conditions. Sci Adv 2021;7:8283–304. https://doi.org/10.1126/SCIADV.ABF8283/SUPPL_FILE/ABF8283_SM.PDF.

[51] Nahid M, Redhwi SSHH, Ali MF. Study on the conversion of waste plastics/petroleum resid mixtures to transportation fuels. J Mater Cycles Waste Manage 2004;6(1):27–34.

[52] Chen Y, Cui Z, Cui X, Liu W, Wang X, Li XinXin, et al. Life cycle assessment of end-of-life treatments of waste plastics in China. Resour Conserv Recycl 2019;146: 348–57.

[53] Perugini F, Mastellone ML, Arena U. A life cycle assessment of mechanical and feedstock recycling options for management of plastic packaging wastes. Environ Prog 2005;24:137–54. https://doi.org/10.1002/EP.10078.

[54] Al-Salem SM, Evangelisti S, Lettieri P. Life cycle assessment of alternative technologies for municipal solid waste and plastic solid waste management in the Greater London area. J Chem Eng 2014;244:391–402. https://doi.org/10.1016/J.CEJ.2014.01.066.